Impaired drainage through capillary-venous networks contributes to age-related white matter loss

Stefan Stamenkovic[1], Franca Schmid[2#], Nicolas Weitermann[1#], Kevin Takasaki[3], Stephanie K. Bonney[1], Maria J. Sosa[1], Yuandong Li[1], Hannah C. Bennett[4], Yongsoo Kim[4,5], Jack Waters[4], and Andy Y. Shih[1,6,7,*]

[1] Center for Developmental Biology and Regenerative Medicine, Seattle Children's Research Institute, Seattle, WA, USA.
[2] ARTORG Center for Biomedical Engineering Research, University of Bern, Freiburgstrasse 3, 3010 Bern, Switzerland
[3] The Allen Institute for Brain Science, Seattle, WA, USA
[4] Department of Neural and Behavioral Sciences, The Pennsylvania State University, Hershey, PA, USA
[5] Center for Neural Engineering, The Pennsylvania State University, University Park, PA, USA
[6] Department of Pediatrics, University of Washington, Seattle, WA, USA.
[7] Department of Bioengineering, University of Washington, Seattle, WA, USA.

* Corresponding author
# These authors share second authorship

Abbreviated title: Impaired capillary and venous drainage in aged brain

Abstract:	150 words
Narrative:	~5300 words (Introduction, Results, Discussion)
References:	49 (9 online methods)
Figures:	8 main (all color); 3 extended; 14 supplementary

Correspondence: Andy Y. Shih
Center for Developmental Biology and Regenerative Medicine
Seattle Children's Research Institute
1900 9th Ave. M/S JMB-5
Seattle, WA 98101
Office: 206-884-1314
Fax: 206-884-1407
Email: Andy.Shih@SeattleChildrens.org

ABSTRACT

The gradual loss of cerebral white matter contributes to cognitive decline during aging. However, microvascular networks that support the metabolic demands of white matter remain poorly defined. We used *in vivo* deep multi-photon imaging to characterize microvascular networks that perfuse cortical layer 6 and corpus callosum, a highly studied region of white matter in the mouse brain. We show that these deep tissues are exclusively drained by sparse and wide-reaching venules, termed principal cortical venules, which mirror vascular architecture at the human cortical-U fiber interface. During aging, capillary networks draining into deep branches of principal cortical venules are selectively constricted, reduced in density, and diminished in pericyte numbers. This causes hypo-perfusion in deep tissues, and correlates with gliosis and demyelination, whereas superficial tissues become relatively hyper-perfused. Thus, age-related impairment of capillary-venular drainage is a key vascular deficit that contributes to the unique vulnerability of cerebral white matter during brain aging.

INTRODUCTION

During brain aging, there is a loss of cerebral white matter that contributes to deterioration of memory and cognitive function.[1] This white matter loss is more severe during progressive age-related diseases, such as Alzheimer's disease and related dementias (ADRD).[2] The dysfunction of the brain's microvasculature, in processes collectively referred to as cerebral small vessel disease (SVD), contributes to white matter loss.[3] Vascular dysfunction precedes detection of amyloid burden, brain atrophy and cognitive decline, suggesting it could be an early driver of loss in brain structure and function.[4] However, there remains sparse literature on how the microvasculature of the white matter differs from gray matter, and why it may be more vulnerable during aging and disease. Small vessel diseases have been most heavily studied in relation to brain arterioles, *i.e.*, arteriosclerosis, lipohyalinosis and cerebral amyloid angiopathy, yet venous drainage systems are equally as important for brain perfusion and remain comparatively understudied.[3]

Forming a basis for deeper investigation of venous function, medullary veins that drain the deep periventricular white matter exhibit increased tortuosity and altered diameter during aging and ADRD, suggesting a role for impaired venous drainage in hypoperfusion and tissue damage.[5,6] However, these deep white matter tracts are not the only to be affected. Recent

studies have shown that the abundant superficial white matter tracts (or U fibers) that support cortico-cortical communication also experience degeneration in ADRD.[7,8] Over four decades ago, Duvernoy and colleagues characterized the microvascular architecture of the human cerebral cortex and U fibers using post-mortem histology.[9] These studies described large, horizontally projecting branches of principal cortical veins/venules (PCVs) within deep cortical layers and underlying U fiber tracts, indicating their substantial influence on blood perfusion in these regions. However, the structure, physiology, and perfusion territories of PCVs remained essentially unstudied. In the mouse brain, white matter tracts of the corpus callosum (CC) are also juxtacortical and support cortico-cortical communication between neighboring cortical regions, similar to human U fibers. The CC has been a major focus for preclinical aging and dementia research because it is the largest white matter tract in the rodent brain.[10] Abnormalities of venular structure and function have been reported in murine models of ADRD[11], but the relation between venules and perfusion of the CC have not been thoroughly examined.

Age is an unavoidable risk factor for ADRD and understanding vascular changes associated with normal aging is a foundational step toward understanding the additive effects of SVD. There is a clear link between age-related changes of the cerebrovasculature and white matter integrity.[12] Blood flow reduction in the white matter of healthy elderly individuals is correlated with the occurrence of white matter lesions.[13,14] Normal aging is also associated with atrophy, gliosis, inflammation, and loss of myelin in white matter tracts.[15] Reduction in vascular density during aging, particularly in white matter, is widely reported and may be the basis for tissue deterioration.[16-18] The etiology of these changes is difficult to understand in the human brain because of limitations in resolution of clinical imaging. This has emphasized a need for *in vivo* preclinical imaging studies that can provide insight on the pathophysiological basis of age-related white matter loss.

To better understand age-related changes in the brain microvasculature, we leveraged recent advances in deep multi-photon imaging that substantially increase imaging depths beyond conventional two-photon imaging by reducing light scattering and out-of-focus excitation.[19-21] These *in vivo* studies were complemented by light-sheet microscopy and *in silico* modeling of the mouse brain vasculature to provide a holistic view of how age-related changes in vascular structure affect cerebral perfusion.[22,23] Our studies provide a framework to discuss angio-architecture in deep cortex and CC, and reveal the physiological dynamics of blood flow and their alterations with aging.

RESULTS

The murine cerebrovasculature contains an equivalent to human PCVs.

In the human cerebral cortex, PCVs exhibit a “Christmas tree”-like branching structure, with a large vertically-oriented trunk and long branches that run along the gray-white matter interface and deeper into the white matter (**Fig. 1a, b**).[9] PCVs are surrounded by rings of penetrating arterioles, suggesting they are the sole output for multiple sources of blood input (**Fig. 1c**). This implicates PCVs as bottlenecks in perfusion of the deep cortex and superficial white matter in humans.

The mouse CC supports cortico-cortical communication similar to human U fibers. To examine whether there is a structural correlate to the human PCV in the murine brain, we performed *in vivo* deep two-photon imaging.[19] This involved use of the far-red intravenous dye (i.v. dye), Alexa 680-dextran, and longer wavelength excitation to achieve deeper tissue penetration than conventional two-photon microscopy (**Fig. 1d**). Imaging was performed on Thy1-YFP mice to provide reference to cortical layers with neuronal labeling (discussed in Material and Methods). We collected high-resolution data sets *in vivo*, averaging 900 μm (x) by 900 μm (y) by 1000 μm (z) in volume, and centered around the main trunk of PCVs in the forelimb, hindlimb, and trunk region of the primary sensory cortex (S1-FL/HL/Tr) (**Fig. 1e, Supplementary Movie 1**). Segmentation of penetrating vessels within this volume confirmed a vascular structure similar to PCVs in human cortex and U fibers (**Fig. 1f, cyan vessel, Supplementary Movie 2**). Murine PCVs extended progressively longer reaching branches with increased tissue depth, and these branches were associated with elaborate microvascular networks of capillaries.

While only one PCV could be observed per imaging volume, the same volume contained 23 ± 3 other ascending venules (**Fig. 1f, dark blue vessels**; n = 9 mice; mean ± SD). However, these other venules terminated at or before cortical layer 5. PCVs represented <4% of all ascending cortical venules and were the only venules that reached the deep cortex and underlying CC. The same tissue volume also contained 15 ± 2 penetrating arterioles, oriented in a ring around the trunk of the PCV, again similar to the human cortex (**Fig. 1g,h**). Approximately 50% of these penetrating arterioles had branches that reached deep cortical layers, ramifying upon reaching the CC. Thus, deeper tissues are served by multiple arteriolar inputs, but rare PCV outputs (**Fig. 1i**).

PCVs are a rare penetrating vessel type draining predominantly from deeper tissues.

To gain a broader view of PCV drainage territories, we surveyed their positions within the cranial imaging window (**Fig. 1j-l**). The main trunk of murine PCVs ascended to the brain surface either at the end of large diameter pial venules (**Fig. 1d, cyan circle**), or at locations hidden beneath large pial venules as they coursed along the surface (**Fig. 1k, cyan circle**). Interestingly, individual PCVs tended to be centered within major representations of primary sensory cortex (S1): FL/HL/Tr, barrel field (BF), and visual (V1) regions (**Fig. 1l**), with one PCV per region. In a 4 mm diameter window, we typically observed 2-3 PCVs. Thus, PCVs may be strategically placed to serve major hubs in cortical function.

To better understand the proportion of penetrating vessel types, we examined light-sheet imaging data collected from whole mouse brains with all vasculature labeled by fluorescent lectin and arterioles with α-SMA and SM22 (**Extended Fig. 1a,b**). The number and penetration depth of all penetrating arterioles (vertically oriented α-SMA-positive vessels), PCVs and other ascending venules (vertically oriented, α-SMA-negative vessels) was examined in 2 mm (x) by 2 mm (y) by 1.2 mm (z) regions of interest in the primary somatosensory cortex, which were ~5-times larger in volume than those examined *in vivo* (**Extended Fig. 1c**). This volume contained on average 55 ± 10 descending arterioles (N = 4 mice; mean ± SD), with a homogenous distribution of termination points across the cortex (**Extended Fig. 1d,e**). There were 105 ± 12 non-PCV ascending venules that terminated with highest density in the upper cortical layers but with some reaching ~900 μm in depth. However, we found only 3.2 ± 0.5 vessels with PCV structure, corresponding to ~3% of total ascending venules.

Defining the structure and nomenclature of PCV regions.

To understand age-related changes in PCV structure, we first imaged adult (5 to 7 months old) and aged (22 to 24 months old) Thy1-YFP mice under isoflurane anesthesia. With both age groups, PCV structure could be consistently visualized up to ~1000 μm of depth *in vivo* (**Fig. 2a-d**). We developed an approach to reliably identify the same vascular zones between animals and in different cortical layers (**Fig. 2e**). The main ascending vessel was denoted the “trunk” of the vessel, and larger vessels directly connected to the trunk were termed “branches”. Branches were numerous and of different diameters, with the largest diameter branches on deepest aspects of the PCV trunk (**Supplementary Fig. 1**). This core branching structure of PCVs did not differ between age groups.

Each PCV branch received blood flow from a dense network of surrounding capillaries, and we characterized these networks in detail. The commonly used strategy of counting vascular branch order from a vertically oriented penetrating vessel trunk in the upper cortex was insufficient

to categorize vessels in deeper networks.[24] This was due to the difficulty in defining a "zero-order" vessel as PCVs ramified into large, horizontally orientated branches. Instead, we relied upon analysis of both microvascular 3D branching structure and blood flow direction. Capillaries closer to arterioles receive blood flow from divergent bifurcations, *i.e.*, transiting blood cells in a single capillary segment will typically supply two downstream branches (**Fig. 2e**, red circles and left insets). On the venular side, capillaries drain into convergent bifurcations as blood flow merges into PCV branches (**Fig. 2e**, blue circles and right insets). Our analyses focused on vessels downstream of the last divergent bifurcation. We defined a capillary sub-type termed the "pre-convergence capillary", which lies between the last divergent and first convergent bifurcation (**Fig. 2f**). Pre-convergence capillaries lie in the middle of the arterio-venous circuit. Downstream of pre-convergence capillaries are other capillary-sized vessels that we collectively termed "other tributary vessels". Other tributary vessels are connected exclusively by points of convergence. Together, pre-convergence capillaries and other tributary vessels form vascular units we termed "tributaries" that drain into the PCV branches at different cortical depths.

We analyzed larger PCV branches and their tributaries in layer 2/3, layer 4 and layer 6/CC (gray-white matter interface) because their microvascular networks were well separated from each other (**Fig. 2g**). Cortical layers 2/3 and 4 were identified using the endogenous Thy1 YFP fluorescence of pyramidal cortical neurons in layer 2/3 and layer 5 (**Supplementary Fig. 2**). As expected, there was a greater complexity in PCV branch structure with increasing cortical depth (**Fig. 2h-j**), with 6.1 ± 2.2, 21.7 ± 5.3 and 24.7 ± 5.6 tributaries per branch in layers 2/3, 4 and 6/CC, respectively (N = 23 mice, aged groups pooled; mean ± SD).

To confirm that layer 6/CC PCV branches were located at the gray/white matter interface, we used *in vivo* three-photon microscopy. Third-harmonic generation (THG) fluorescence from myelin allowed precise determination of the gray-white matter interface, where vertically oriented myelin fibers of descending axonal projections from the cortex transitioned into horizontally oriented fiber bundles of the CC (**Fig. 2k)**. Simultaneously, intravenously injected FITC-dextran (i.v. dye) was used to visualize vascular structure up to 1000 μm from the pial surface (**Fig. 2l**). These data confirmed that layer 6/CC PCV branches were located at the gray-white matter interface (**Fig 2m**, punctuated THG signal on the left) and extended deeper into the CC (**Fig 2m**, striated THG signal on the right)**.** Thus, layer 6/CC PCV branches drain blood from cortical layer 6 and the underlying CC (**Fig. 2n**), and deep two-photon imaging can reach these tissue depths *in vivo*.

Simplification of tributary structure due to age-related regression of pre-convergence capillaries.

We next characterized PCV tributaries by assessing their network architecture. Pre-convergence capillaries were the predominant vessel type in PCV tributaries, as they represented 60.12 ± 1.47% of the total vessel segments (N = 23 mice; mean ± SD) and 81.60 ± 4.95% of the total vessel length (N = 23 mice; mean ± SD)(**Fig. 3a, b**). Interestingly, in aged mice, the percent of total vessel segments and vessel length corresponding to pre-convergence capillaries increased (**Fig 3c**), and this difference was most prominent in layer 6/CC (**Supplementary Fig. 3a, b**). Yet, we detected a ~10% reduction in vascular length density (**Fig. 3d,e**, **Supplementary Fig. 3c,d**) and number of vessel segments per PCV tributary in layer 6/CC (**Fig. 3f**). We further detected a shift in tributaries from higher to lower complexity across all three layers in aged animals (**Supplementary Fig. 3e-g**). These findings suggest that age-related regression of pre-convergence results in simplified tributary structures in layer 6/CC, and to some extent in all cortical layers.

We developed a hypothesis for how simplification of tributary structure may be occurring (**Fig. 3g**). Age-related regression of pre-convergence capillaries (**Fig. 3g,** gray asterisks) reduces vascular density and the number of vessels forming the tributaries. The remaining pre-convergence capillaries would then become a single, longer and more tortuous capillary segment (**Fig. 3g,** red asterisk). The segment would still be classified as a pre-convergence capillary since it lies between the last point of divergence and first point of convergence. This would change the ratio in the number of pre-convergence capillaries relative to other tributary vessels. The observed increase in pre-convergence capillary number and length in PCV tributaries of aged mice is therefore consistent with this postulation (**Fig 3c**).

We next considered potential causes of age-related pre-convergence capillary regression. Given their mid-capillary bed location, they are the capillaries with the lowest blood flow in the arterio-venous circuit.[25] Low flow increases the chance of blood flow stalling, often due to transient plugging by white blood cells[26], which can in turn cause capillary regression with prolonged flow arrest.[17,27] During *in vivo* imaging, we observed capillaries lacking movement of blood cell shadows, *i.e.*, blood flow stalls (**Fig. 3h,** white arrow). Blood flow stalls were relatively low in number across all tributaries (0.57 ± 0.16% across all data from both age groups; N = 23 mice; mean ± SD). However, nearly all flow stalls (92.5%) occurred in pre-convergence capillaries (**Fig. 3i**). Moreover, instances of spontaneous pre-convergence capillary regression were observed in separate imaging sessions, 7-14 days apart, and these always occurred in vessels that had

exhibited stalls or very low blood flow during prior imaging (**Fig. 3j**). These observations suggested that flow stalls are linked to pre-convergence capillary regression.

Altered structure and hemodynamics of pre-convergence capillaries of aged mice.

Given the vulnerability of pre-convergence capillaries during aging, we further dissected their structure across cortical layers at the level of individual capillary segments (**Fig. 4a,b**). Again, consistent with our hypothesis above, we detected a significant increase in both pre-convergence capillary length and tortuosity in aged mice in layer 6/CC, at the level of individually quantified vessels (**Fig. 4d,e**). Critically, these analyses revealed that pre-convergence capillary diameter was significantly reduced in aged animals, with a 2.1% reduction in layer 4 and a pronounced 7.1% reduction in layer 6/CC (**Fig. 4f**). Since small changes in capillary diameter can have profound effects on blood flow[28,29], we measured red blood cell (RBC) flux, velocity, and linear density in individual capillaries across entire PCV branch networks using line-scans (**Fig. 4a, c**). Assessment of 6500 capillaries across 23 mice revealed a pronounced age and layer-specific reduction of RBC flux and velocity in layer 6/CC pre-convergence capillaries (**Fig. 4g, h**).

We also examined RBC linear density, which reports the instantaneous spatial distribution of blood cells per capillary segment and is akin to hematocrit. Linear density was reduced across all layers in aged animals, and this was most evident in layer 4 and layer 6/CC (**Fig. 4i**). This may in part reflect overall reduction in blood hematocrit with age. Surprisingly, we also observed an increase in RBC flux and velocity in layer 2/3 and layer 4 of aged mice (**Fig. 4g, h**), suggesting that flow resistance in layer 6/CC causes a redistribution of blood flow into upper cortical layers during aging. Capillary length, diameter and flow also exhibited graded increases with cortical depth, which was presumably critical for allocation of blood to deeper tissues. However, this depth dependence was dampened in aged mice (**Extended Fig. 2**). These data suggest that age-related hypoperfusion is regional, affecting primarily layer 6/CC, while layer 2/3 exhibits a contrasting hyper-perfusion. This emphasizes the need to obtain a holistic view of blood flow across all cortical layers to understand the basis of cerebral hypoperfusion.

We next examined how aging affected other tributary vessels downstream. Unlike pre-convergence capillaries, no age-related differences were observed in average length and tortuosity, likely due to the shorter lengths of these vessel segments (**Supplementary Fig. 4a-d**). However, age-dependent constriction of vessels in layer 4 and 6/CC, and altered cortical depth dependence of diameter, was also seen in other tributary vessels (**Supplementary Fig. 4e, f**). RBC flux, velocity, and linear density in other tributary vessels also showed similar age-related

changes seen with pre-convergence capillaries (**Supplementary Fig. 5**). Finally, we extracted heart-rate from RBC velocity data and found no major differences between age groups, suggesting that the observed blood flow differences were not due to altered cardiovascular status in aged mice (**Supplementary Fig. 6**). Collectively, our data suggest that vasoconstriction and reduced blood flow occurs broadly in layer 6/CC tributaries, but pre-convergence capillaries are most vulnerable to blood flow stalling and regression.

Age-related reduction in layer 6/CC blood flow is not due to change in arteriolar diameter.

Reduced blood flow in deep cortical PCV vascular networks could be caused by constriction of penetrating arterioles. We therefore also examined the diameter of arterioles that reached layer 6/CC (**Supplementary Fig. 7a, b**). In deep tissues, cortical penetrating arterioles terminate and ramify into smaller arteriolar branches. We measured both the main trunk of penetrating arterioles and their branching arterioles. No significant difference between adult and aged mice was detected (**Supplementary Fig. 7c**), supporting the idea that vasoconstriction in PCV tributaries was the primary driver of reduced blood flow. We also considered pre-capillary sphincters given their recent implication of age-related perfusion deficits during neurovascular coupling.[30] However, we were unable to identify structures with distinct sphincter and bulb like structure in the branching arterioles of layer 6/CC, which are more apparent in the upper cortex.

Aging related changes in PCV vascular networks are not a consequence of anesthesia.

While convenient for structural imaging, isoflurane is a vasodilator that can alter hemodynamics.[31] We therefore also imaged a cohort of adult and aged mice first under isoflurane anesthesia, and on a separate day, in the awake state with free mobility on a treadmill (**Fig. 5a**). The mice were gradually habituated to head fixation prior to data collection, and similarity in heart rate between the anesthetized and awake states suggested no overt differences in cardiovascular status (**Fig. 5b**). These studies revealed a similar age-related hypoperfusion in deeper tissues of awake mice, with some noteworthy differences (**Fig. 5c-e**). Capillary diameter was significantly reduced in layer 6/CC of aged mice, but lack of anesthesia revealed increases in capillary diameter in layers 2/3 and 4 (**Fig. 5c**). Again, consistent with redistribution of blood flow into upper cortical layers, RBC flux was reduced in layer 6/CC of aged animals, and an increase was detected in layer 2/3 (**Fig. 5d**). RBC velocity was unchanged in layer 6/CC, but increases were still observed in layers 2/3 and 4 of aged mice (**Fig. 5e**). RBC linear density was decreased in all cortical layers of aged, awake mice (**Fig. 5f**), whereas it was most prominent in deeper layers during anesthesia. Cortical depth-dependent increases in vasodynamic parameters were also

dampened in awake, aged mice (**Extended Fig. 3**), just as seen with anesthetized mice. Thus, the key finding of age-related impairment of blood flow in layer 6/CC and its redistribution towards upper cortical layers holds irrespective of anesthesia state.

Altered reactivity of capillary diameter across cortical layers with aging.

We also leveraged isoflurane's vasodilatory effect to probe for age-related differences in capillary reactivity. Compared to the awake state, isoflurane increased RBC flux and velocity in all layers, with the largest increases in layer 6/CC (**Supplementary Fig. 8a, b, e**). A similar magnitude of blood flow increase was seen with both age groups, suggesting a general preservation of reactivity. However, some layer-specific differences were noted with aging. Aged mice exhibited significant increases in RBC linear density in layers 2/3 and 4, as opposed to a selective increase in layer 6/CC for adult mice (**Supplementary Fig. 8c, e**). Further, aged mice showed a strong dilation of only layer 2/3 capillaries, whereas adult mice exhibited modest dilations in layer 2/3 and strong dilations in layer 6/CC (**Supplementary Fig. 8d, e**). Altogether, these results suggest that diminished capillary reactivity in deep layers, alongside increased reactivity in upper layers, contributes to age-related blood flow redistribution across layers.

Vessel diameter is the main determinant of capillary flow in PCV networks.

To examine which age-related changes in vascular structure were drivers of hemodynamic change, we performed Pearson correlation analyses between the structural and functional properties of individual tributary vessels in the anesthetized (**Supplementary Fig. 9 and Supplementary Table 1**) and awake state (**Supplementary Fig. 10 and Supplementary Table 2**). Vessel tortuosity was not correlated with hemodynamic parameters in any condition, while both the length and diameter of both pre-convergence capillaries and other tributary vessels showed strong correlation with RBC flux. Between these parameters, vessel diameter showed the strongest correlation. Thus, while other vascular alterations upstream or downstream can affect capillary flow, these data suggest that local capillary constrictions during aging strongly influence capillary network perfusion.

In silico modeling of age-related change in vascular structure recapitulates in vivo findings.

To determine whether the degree of capillary constriction and rarefaction observed *in vivo* was sufficient to explain blood flow deficits seen with aging, we performed blood flow simulations in realistic microvascular networks derived from mouse parietal cortex.[23] The *in silico* model is

well-established and uses Poiseuille's Law and the continuity equation to compute the pressure field and flow rates for all vessels[23]. Moreover, the model accounts for the presence of red blood cells and their effect on the flow field[32] (see Methods for additional details).

Four cases were studied in two microvascular networks, each involving reduction in the diameter and/or density of select capillaries in layer 6/CC (800 to 1000 μm of cortical depth) (**Fig. 6a**). To mimic the *in vivo* scenario, we constricted all capillaries by 7%, which was the average detected *in vivo* in our larger data set from aged, anesthetized mice. To determine which capillaries to trim from the network for density reduction, we examined the distribution of pre-convergence capillary lengths and found that capillaries shorter than 70 μm tended to be lost in aged mice (**Supplementary Fig. 11**). We selectively trimmed from the network capillaries with similar attributes near the center of the arteriovenous axis where pre-convergence capillaries are generally located.

These network modifications caused most capillaries in layer 6/CC to reduce in blood flow (50-60%), while a very small proportion of diffuse capillaries increased in blood flow (0.3% of capillaries) (**Fig. 6b**). In the remaining fraction of capillaries, the relative change from baseline was smaller than 10%. On average, there was a significant reduction of average RBC flux, velocity and linear density in layer 6/CC at magnitudes similar to that detected *in vivo* (**Fig. 6c-e**). Further, these changes were sufficient to reduce total blood inflow and outflow through arteriolar and venular branches in layer 6/CC, respectively (**Fig. 6f, g**). Although we also observed a slight increase of flow in upper cortical layers, these changes were more modest compared to the *in vivo* findings. This suggests that redistribution of blood flow into upper cortical layers *in vivo* is not necessarily a passive result of increased vascular resistance in layer 6/CC but may involve active dilatory mechanisms that are not captured *in silico*.

When the effects of capillary constriction and density reduction were examined separately, we found that the parameters had independent influences on RBC flux (**Supplementary Fig. 12a-c**). Reduction of vascular density had a stronger effect on RBC velocity (**Supplementary Fig. 12d-f**), while capillary constriction exerted a greater influence on RBC linear density (**Supplementary Fig. 12g-i**). Collectively, these data suggest that both capillary constriction and reduced vascular density are sufficient to drive hypoperfusion in aged PCV tributaries.

Age related reduction in deep cortical blood flow is coupled with white matter gliosis and demyelination.

To determine whether age-related hypoperfusion in layer 6/CC was associated with tissue changes in layer 6/CC, we examined for immunohistochemical markers of gliosis (Iba1, GFAP) and myelination (myelin basic protein) in a cohort of adult and aged mice previously used for *in vivo* imaging. This revealed foci of microgliosis (**Fig. 7a-c**), astrogliosis (**Fig. 7d-f**), and demyelination (**Fig. 7g-i**) most notably within the CC of aged mice. This suggests that impaired drainage through PCV networks contributes to age-related loss of white matter integrity.

Decreased capillary pericyte density in layer 6/CC of aged mice.

Pericytes are mural cells that line brain capillaries and their contraction can lead to a reduction in capillary blood flow.[24,33] Further, experimentally inducing pericyte loss causes capillary blood flow stalling, reduction in capillary structure, and white matter degeneration.[34-36] We therefore examined how aging affected pericyte density across different cortical layers and the CC. We revisited light-sheet data obtained by imaging of whole mouse brains (**Fig. 8a-d**) and broadened our analyses to young adult (2 months old) and aged (24 months old) mice. Vascular length density and pericyte numbers (visible by their protruding somata) were examined in ROIs centered on the primary somatosensory cortex, which were further divided into 200 μm (z) thick subsections (**Fig. 8e-j**). This revealed an age-related reduction in vascular length density and pericyte numbers starting from 400 μm of intracortical depth, which is approximately where layer 4 PCV branching networks are located (**Fig. 8k, l**). When pericyte numbers were normalized to the total vascular length, a specific age-related reduction in pericyte density was detected at 800-1000 μm of depth, corresponding to layer 6/CC (**Fig. 8m**). Together, these data point to pericyte dysfunction in layer 6/CC during aging that may contribute to capillary constriction and regression.

DISCUSSION

Cerebral white matter is uniquely vulnerable to hypoperfusion and injury during aging, yet the microvascular networks that support white matter have remained poorly defined. Using deep multi-photon imaging, we show that cortical layer 6 and CC, the most widely studied white matter tract in the murine brain, is drained by rare and wide-reaching penetrating venules called PCVs. We observed constriction and rarefaction of capillaries in the deep branching networks of PCVs, which caused selective hypoperfusion of layer 6/CC. This regional hypoperfusion was associated with gliosis and myelin loss. In contrast, upper cortical layers experienced increased blood flow with aging due to redistribution of blood across cortex. These findings implicate deep PCVs branches as bottlenecks in perfusion of white matter and contributors to age-related white matter loss. Given strong similarites in vascular architecture between murine layer 6/CC and the human

cortical-U fiber interface[9], similar age-related changes may contribute to degeneration of superficial white matter in humans.

Loss of capillary density is well documented in studies of rodent[17,37] and human brain vasculature[38], but few have related this loss to specific locations within the 3D vascular architecture. Our structural analyses identified pre-convergence capillaries as a site of vulnerability in age-related capillary rarefaction. Pre-convergence capillaries are the middle of the arterio-venous circuit, and their lower basal flow may increase susceptibility to plugging by blood cells, particularly during vasoconstriction. We found that regressed capillaries were those that previously stalled or supported very low blood flow, and this relation strengthens a growing link between blood flow stalling/obstruction and capillary regression during aging.[17,27,34] The mechanism of capillary stalling in deep tissues remains to be clarified. Our *in silico* modeling and prior *in vivo* studies[24] suggest that the observed constriction of 7% (anesthetized) and 14% (awake) is sufficient to slow blood cell flow. However, increased prevalence of adherent leukocytes with pericyte loss may also be a factor.[36]

Aging alters the distribution of blood flow across cortical depths. In adult mice, we observed consistent, layer-dependent increases in blood flow. This gradation was dampened in aged mice because of reduced flow in deep tissues and increased flow in upper cortex. These findings align with previous reports of both increases[39] and decreases[40] in blood flow with brain aging, and explain how these conditions co-exist, but at different cortical depths. Our observation of age-related capillary dilation in upper cortex is also consistent with prior work.[30] This dilation likely contributes to maldistribution of blood from deep tissues to upper cortex. The maintenance of higher blood flow rates in deep tissues is presumably needed to compensate for reduced oxygen content as RBCs travel further from the arterial source. Consistent with this, an *in vivo* study by Li et al. showed depth-dependent decreases in partial oxygen pressure (pO_2) in penetrating arterioles and ascending venules.[41] We suspect that a ~20% reduction in RBC flux in layer 6/CC of aged mice reduces pO_2 to levels that challenge metabolic function in white matter. When combined with greater inter-capillary distance caused by rarefaction, this may lead to pockets of tissue hypoxia[42] and increased susceptibility to secondary insults. In the context of AD risk factors (Apoe4), additional vascular insufficiencies increases tissue hypoxia in the CC, as detected by hypoxyprobe.[10] The level of pO_2 decrease that occurs with normal aging of the CC remain to be clarified. Non-invasive *in vivo* approaches to measure pO_2 at depth remain limited, and hypoxyprobe may not detect hypoxia if below threshold for detection. However, the

observation of gliotic reactions in the aged CC has been consistently observed in aging studies.[43] and suggests that myelin loss is not simply a result of age-related brain atrophy.

The mechanism of capillary constriction will be an important but challenging question to address. Pericytes were a focus in this study because their loss has been shown in clinical neuropathological studies of the aged brain[35,44], and experimentally induced pericyte loss impairs blood flow and promotes capillary regression, as well as blood-brain barrier dysfunction with more severe loss.[34,35,45,46] However, the roles of pericyte dysfunction in the natural progression of aging and disease remain difficult to dissect without more selective tools to genetically target brain pericytes, preferably in a region-specific manner. As such, most studies remain correlative. Our study is not unique in this regard but adds new insight on capillary perfusion in regions experiencing natural pericyte loss. It is possible that pericytes abnormally contract during aging of the white matter due to membrane depolarization and calcium influx, or increased production of vasoconstrictive agonists (endothelin-1, thromboxanes).[47] We also cannot rule out other potential factors, such as changes in the structure of the endothelium[48] or other perivascular structures. However, the *in vivo* imaging techniques employed here make it possible to assess therapeutic and physiological manipulations that can rescue age- and disease-related blood flow deficits in white matter. Indeed, we find that deep capillaries in the aged brain remain quite reactive to vasodilatory stimuli (isoflurane), and may therefore be amenable to clinically used therapeutics with known vasodilatory actions on pericytes and capillaries.[24,49] Similarly, life-style changes such as exercise have also recently been shown to rescue age-related blood flow deficits in the CC.[40]

From the vantage point of preclinical murine studies, deep multi-photon imaging is poised to reveal new insights into the etiology of cerebrovascular disease, which can inform human studies. Our study builds a framework to navigate the distinct microvascular networks of the deep cortex and CC in murine experiments, which is essential for consistent measurements within and across animals. We established baseline to understand microvascular change in disease models involving an aging component. Further, our data emphasizes the importance of gaining a holistic view of blood flow changes across cortical layers, since a limited view of the upper cortex results in an incomplete understanding of blood flow deficit. Coupled with the broad view provided by light-sheet microscopy[18], *in vivo* studies can now hone into specific brain regions most vulnerable during aging and disease.

METHODS

Mice. All procedures in this study were approved by the Institutional Animal Care and Use Committee at the Seattle Children's Research Institute. The institution has accreditation from the Association for Assessment and Accreditation of Laboratory Animal Care (AAALAC), and all experiments were performed within guidelines. The study was performed on adult (n = 12; 6 male and 6 female, 5 to 7-month old) and aged (n = 12; 9 male and 3 female, 22 to 24-month old) Thy1-YFP mice bred on the C57Bl/6 background (B6.Cg-Tg(Thy1-YFP)HJrs/J; Jax ID 003782). Age group ranges were determined by the Jax "Life Span as a Biomarker" criteria, which defines 3-6 months as "mature adult" stage, and 18-24 months as "old" stage in mice. Aged mice were visually checked for general health and any overt signs of illness such as tumors or weight loss resulted in exclusion from the study. The mice were housed on a 12-h light (6:00 to 18:00), 12-h dark cycle, with *ad libitum* access to chow and water. The use of adult and aged mice was interleaved over the entire period of study.

Chronic cranial windows. Dexamethasone (40 µl; Patterson Veterinary) was subcutaneously administered to animals 4 h prior to the surgery, which helped to reduce brain swelling during the craniotomy. Anesthesia was induced with a cocktail consisting of fentanyl citrate (0.05 mg/kg), midazolam (5 mg/kg) and dexmedetomidine hydrochloride (0.5 mg/kg) (Patterson Veterinary). Under sterile conditions, the scalp was excised, and the periosteum cleaned from the skull surface. An aluminum flange for head fixation was attached to the right side of the skull surface using the C&B-Metabond quick adhesive cement (Parkell; S380). A circular craniotomy (dura left intact), ~4 mm in diameter, was created over the left hemisphere and centered over 2-mm posterior and 3-mm lateral to bregma encompassing the primary somatosensory cortex. The craniotomy was sealed with a glass coverslip plug consisting of a round 4 mm glass coverslip (Warner Instruments #64-0724) glued to a round 5 mm coverslip (Warner Instruments #64-0731) with UV-cured optical glue (Edmund optics #37-322). The coverslip was positioned with the 4 mm side placed directly over the craniotomy, while the 5 mm coverslip laid on the skull surface at the edges of the craniotomy. Loctite Instant Adhesive 401 was carefully dispensed along the edge of the 5 mm coverslip to secure it to the skull. The area around the cranial window was then sealed with dental cement. Throughout surgery, body temperature was maintained at 37˚C with a feedback-regulated heat pad (FHC Inc.), and the mice were provided oxygenation through medical air (20–22% oxygen and 78% nitrogen, moisturized by bubbling through water; AirGas Inc.). Imaging was initiated after a 3-week recovery period.

In vivo deep two-photon imaging (isoflurane anesthesia). Mice were maintained under light isoflurane anesthesia (~1.5% minimum alveolar concentration) delivered by medical air (20–22% oxygen and 78% nitrogen, moisturized by bubbling through water; AirGas Inc.), and body temperature was maintained at 37˚C with a feedback-regulated heat pad (FHC Inc.) throughout the imaging period. To label the vasculature, 100μl of 5% (w/v in sterile saline), 2MDa Alexa 680-dextran was injected through the retro-orbital vein. Alexa 680-dextran was custom conjugated using a previously published protocol.[19] *In vivo* two-photon imaging was conducted using a Bruker Investigator microscope (run by Prairie View 5.5 software) coupled to a Spectra-Physics Insight X3 laser source (SpectraPhysics). Endogenous YFP fluorescence and Alexa 680-labeled microvasculature was imaged at 900 nm and 1210 nm excitation, and emission was collected through 525/70-nm and 700/75-nm bandpass filters, respectively. During imaging laser power ranged between 4 and 145 mW exiting the microscope objective, with higher powers required for greater cortical depth (**Supplementary Fig. 13**).

Imaging timeline. Each mouse underwent 5 sessions of *in vivo* deep two-photon imaging under anesthesia with <2.5 h of imaging time per session and 2-3 days between the sessions. During the first imaging session, low-resolution maps of the cranial window were collected using a 4-X 0.16 numerical aperture (NA) objective (Olympus; UPlanSAPO) for navigational purposes, as well as to identify PCV locations. Once the appropriate PCV was located, high-resolution imaging of PCV branches and associated microvascular networks was performed through the entire cortical depth. Image stacks were collected using a 25-X, 1.05 NA water-immersion objective lens (XLPlan N, Olympus) across a 483x483 μm field of view with lateral sampling resolution (x, y) of 0.943 μm/pixel and axial sampling resolution (z) of 1 μm/pixel. Two to four image stacks were often collected and stitched using an ImageJ/FIJI “Pairwise stitching” plugin to cover the region of interest.[50]

We analyzed PCV branches originating directly from the main PCV trunk between 200 – 400 μm, 400 – 600 μm and 800 – 1000 μm of intracortical depth, roughly corresponding to cortical layers 2/3, 4 and 6/CC, respectively (**Fig. 2c**). Branches at these depths drained blood from non-overlapping regions and generally covered upper, mid and deep layers of the cortex. To confirm the location of cortical layers 2/3 and 4 we examined endogenous fluorescence in pyramidal neurons of layers 2/3 and 5 (**Supplementary Fig. 2**). 3D visualization of high-resolution Z-stacks was performed using Imaris software version 7.7.2 (Bitplane, Oxford Instruments). Vascular segments presumed to belong to a PCV branch network were identified based on the evaluation of vascular structure from the obtained stacks. To ensure that we were including the correct

starting points of the networks, all vessel segments starting from one branch order upstream of the putative starting points of the PCV network and downstream to the main branches of the PCV were marked. Then, the location of the marked vascular segments was labeled in the original Z-stack using ImageJ/FIJI to provide a map of where line scanning was to be performed in subsequent imaging sessions.

Line scan data acquisition. During *in vivo* deep two-photon imaging sessions 2, 3 and 4 under anesthesia, line scan data were collected from vessel segments in line scan maps from layer 2/3, 4 and 6/CC (one cortical layer per session). Line scanning was performed using the 25-X, 1.05 NA water-immersion objective lens (XLPlan N, Olympus) and 3-X digital zoom was used to guide accurate placement of the line scan. Vessel segments were sampled individually with line scan duration set to ~1.2 s at a sampling frequency of ~2 kHz. During acquisition of line scan data, we also followed the number of stalled vessel segments. Vessel segments were considered stalled if they had no blood flow for more than 20 minutes, and these vessels were reassessed periodically over the imaging session. To ensure that the laser powers used for line scans did not directly induce damage or alter blood flow, we longitudinally imaged the same population of Layer 6/CC vessels weekly for 5 weeks in a cohort of mice (**Supplementary Fig. 14**). We observed no overt signs of vascular damage, *i.e.*, dye extravasation indicative of blood-brain barrier damage or vascular regression. Blood flow was consistent and unperturbed across all time points examined.

Analysis of the PCV main branches. During *in vivo* deep two-photon imaging session 5, we collected high-resolution Z-stacks through the entire cortex, starting at the pia mater and ending at ~1000 μm of cortical depth. Lateral sampling (x, y) was 0.943 μm/pixel, and axial sampling (z) was 1 μm/pixel. As mentioned above, to capture the entire branching structure of the PCV we collected and stitched 4 adjacent and partially overlapping z-stacks arranged in a 2x2 square formation, with the main PCV trunk set in the center. Using the stitched Z-stacks, we analyzed the overall branching structure of PCVs in adult and aged mice. We measured the diameter of each PCV branch segment right next to the point where it joins the main trunk of the PCV, as well as the cortical depth at which the branch originates. Furthermore, we analyzed the number of PCV branches through cortical depth, after binning in 200 μm depth groups.

Awake imaging. A subset of Thy1-YFP mice (n = 5 adult, 2 male and 3 female; and n = 6 aged, 5 male and 1 female) was imaged both under isoflurane anesthesia (as described above) and in the awake state. During awake imaging, mice were head fixed and allowed to freely move on a low resistance treadmill (Phenosys SpeedBelt). All mice were habituated for head fixation over 3

training sessions (each ~2 days apart) where mice were head-fixed on the treadmill and placed in the light-shielded microscope cage with the objective over the cranial window to imitate the conditions during imaging. The mice were then held in the imaging setup for 20 min before being returned to the home cage. After training, each mouse underwent 7 imaging sessions over 3.5 weeks (2 imaging sessions per week, 3 days apart). The first session was performed under isoflurane anesthesia to collect low-resolution maps of the cranial window for navigational purposes, as well as to identify the location of PCVs, as described above. Once the appropriate PCV was located, high-resolution imaging was performed throughout the entire depth around the PCV. In the following 6 imaging sessions, line scan data were collected from vessel segments from layer 2/3, 4 and 6/CC (one cortical layer per session). We alternated imaging of the same cortical layer in the awake state and under anesthesia on separate sessions in immediate succession to obtain hemodynamic data from the same population of vessels under both conditions. At the end of each awake imaging session a Z-stack of the imaged PCV vascular network was collected for analysis of vessel diameter.

Defining the vascular networks of a PCV branch. We defined that PCV branch networks should include all vessel segments that converge blood flow towards that branch. Therefore, we considered the last points of blood flow divergence within the capillary network as the starting points for the PCV branch vascular network. By using 3D structural information from our image stacks and blood flow directionality information from our line scan data we were able to reliably identify the last points of convergence in the analyzed PCV vascular networks.

The first vessel segments in the PCV branch vascular network are located between the points of divergence on one end and the points of convergence on the other. We named these vessel segments as “pre-convergence” capillaries. Pre-convergence capillaries merge and form a system of downstream convergent vessel segments that eventually lead to the PCV branch. We named these downstream convergent vessels “other tributary vessels”. Pre-convergence capillaries and other tributary vessels form distinct systems of vessels termed “tributaries” that converge blood flow into the PCV branch. By analyzing the branching structure of PCV vascular networks we found that tributaries consist of up to 4 branching orders of vessel segments starting from the last point of blood flow divergence. Therefore, pre-convergence capillaries are first order vascular segments, while other tributary vessels may form up to 3 additional orders of vascular segments beyond the last point of blood flow divergence. All vessel segments above branching order 4 were considered a part of the PCV branch. Therefore, the vascular network of a PCV

branch consists of the branch segment and a system of tributaries of differing complexity that flow into the branch (**Fig. 2e, f**).

Analysis of tributary structure. As the capillary network is predominantly composed of bifurcating branchpoint, the number of vessel segments in tributaries is almost always an odd number. The simplest tributaries consist of single pre-convergence capillaries. Tributaries containing two branching orders of vessels in their structure have 3 vessel segments, those containing three branching orders have 5 or 7 vessel segments, and those containing four branching orders have 9, 11, 13 or 15 vessel segments **(Fig. 3h)**. To analyze tributary structure, we measured the average number of vessel segments per tributary and separated tributaries into 3 groups: low (1 or 3 vessels), medium (5 or 7 vessels) and high (9 or more vessels) complexity. In case of a tributary containing a trifurcation point and consisting of an even number of vessel segments, it was categorized as the first higher odd number tributary (i.e., 4 as 5, 6 as 7 etc.). We then calculated the percentage ratio of each complexity group in the tributary populations of our PCV vascular networks. For each analyzed PCV vascular network, we calculated the total number of tributaries belonging to a certain complexity group (low, medium, high) and expressed it in relation to the total number of tributaries in the PCV network (**Supplementary Fig. 3e-g**).

Segmentation of PCV vascular networks. Vascular networks of PCV branches in Z-stacks were reconstructed in 3D using the Imaris, version 7.7.2 (Bitplane, Oxford Instruments). Vessel segmentation was performed manually using the “Auto Depth” tracing option in the Filament Tracer module of Imaris. “Center” and “Smooth” options in the Edit tab of the Filament tracer module were used to correct for any tracing mistakes. After segmentation of the networks, the length and straightness for each reconstructed vessel segment were extracted from the Statistics tab of the Filament tracer module. The straightness values reported by the software are directly reciprocal to tortuosity.

Vessel diameter. Lumen diameter of different vessel types was measured in maximally projected images from high-resolution Z-stacks. 10 μm of thickness was projected for the analysis of capillary diameter and smaller PCV branches, while 20-40 μm of thickness was projected for analysis of larger PCV branches. To reduce bias of measurement location, we used a custom ImageJ/Fiji macro called VasoMetrics to analyze lumen full-width at half maximum diameter at multiple, equidistant locations (spaced 1 μm) along each vessel segment of interest.[51] The values across each vessel segment were used to calculate the average diameter of the vessel and the standard deviation of diameter along the measured region.

Quantification of hemodynamic parameters and stalled vessels. For each line-scan captured, we calculated RBC flux by manually counting the number of blood cell shadows over the total duration of the line scan and normalizing all numbers to represent blood cells transiting in a period of 1 second. The angle of the streaks in relation to the direction of the scan was used to determine RBC flow direction. Analysis of blood flow velocity and heart rate was performed using a previously published MATLAB algorithm.[52] Linear RBC density values for each vessel segment were calculated by dividing the RBC flux with the blood flow velocity. Blood flow stalls were identified as capillaries lacking moving blood cell shadows for at least a period of 20 min during repeated observations within the same imaging session.

Analysis of vascular density. Analysis of vascular density was performed in two ways using the Imaris software. First, we assessed vascular density (total vascular length per volume) in regions enriched with pre-convergence capillaries. This involved placing 6 small regions of interest (100 x 100 x 100 μm (x, y, z)) within each reconstructed PCV network (**Fig. 3e, f**). Second, vascular density was measured more broadly in cortical layers by assessing larger regions of interest (300 x 300 x 100 μm (x, y, z)) within layers 2/3, 4 and 6/CC (**Supplementary Fig. 3c, d**). Two ROIs were analyzed per each layer, for a total 300 x 300 x 200 μm (x, y, z) ROI volume.

In vivo three-photon imaging. A subset of adult C57BL/6 mice (n = 3, 2 male and 1 female) was imaged using *in vivo* three-photon microscopy. A representative example is shown in **Fig. 2h-n**. First, a chronic cranial window was implanted over the somatosensory cortex. Briefly, under 0.5–2% isoflurane anesthesia, a head restraint bar was attached to the skull using C & B Metabond (Parkell) and a circular craniotomy 5-mm in diameter was opened over the left visual cortex at coordinates 2.7 mm lateral, 3 mm posterior to bregma. A durotomy was performed and the craniotomy was sealed with a plug consisting of a stack of three #1 coverslips (two round 5 mm coverslips and one round 6 mm coverslip), attached to each other using optical adhesive, and attached to the skull with Metabond. Use of the 3-layered cranial window plug prevented subsequent skull regrowth but may occasionally cause slight compression of the cortical tissue thus causing small reduction in measured cortical thickness.

Imaging was performed on a three-photon microscope built around a Coherent Monaco/Opera-F laser source (≤2 nJ, 50 fs pulses at 1 MHz; Coherent Inc.) and a modified MIMMS microscope manufactured by Sutter Instrument. The scan and tube lenses were replaced (Thorlabs SL50-3P and a Plössl pair of achromatic doublets, Thorlabs AC254-400-C, respectively) to improve transmission at 1300 nm. The primary dichroic mirror was FF735-DI02 (Semrock). Nikon 16×/0.8 objective (50% transmission at 1300 nm) was used, and image

acquisition was controlled by ScanImage (Vidrio Technologies LLC) with acquisition gating for low repetition rate lasers. Animals were imaged in the awake state. To label the vasculature, prior to imaging mice were injected with 100µl of 5% (w/v in sterile saline) 2 MDa dextran-FITC through the retro-orbital vein under a brief period of isoflurane anesthesia. Emitted green fluorescence was separated from incoming excitation light by a dichroic beam splitter (FF735-Di02, Semrock), then filtered by a bandpass filter (ET525-70m-2p, Chroma). Third harmonic generated (3HG) signal produced by blood vessels and myelinated axons was detected using a secondary dichroic beam splitter (Di02-R488, Semrock) and filtered by a bandpass filter (ET434/32m, Chroma) into a separate blue channel which allowed us to clearly discern the gray-to-white matter boundary.[53]

Tissue clearing and 3D immunolabeling for light-sheet imaging. Whole brain 3D light sheet fluorescence microscopy imaging was conducted at the Pennsylvania State University (PSU) and approved by the Institutional Animal Care and Use Committee at PSU. Four (2 male and 2 female) 2-month-old (young) and four (2 male and 2 female) 24-month-old (old) C57BL/6J mice were used in the study. The iDISCO+ tissue clearing protocol was used with modifications.[18,54] Brain samples were delipidated in SBiP buffer, consisting of ice-cold water, 50mM Na2HPO4, 4% SDS, 2-methyl-2-butanol and 2-propanol. This buffer becomes activated at room temperature and was therefore made and stored at 4°C prior to use. Each sample was submerged in 10 mL of SBiP buffer, rotated at room temperature with buffer changes at 3 hours, 6 hours and then incubated with fresh SBiP buffer overnight. For adequate delipidation, particularly with aged samples, each brain was then washed with SBiP for a total of 6 days, with daily buffer changes. After delipidation, brain samples were washed with B1n buffer, which consists of 0.1% Triton X-100, 1g of glycine, 0.01% 10N NaOH and 20% NaN_3. Brain samples were washed with 10 mL of B1n buffer at room temperature for 2 days.

To begin immunolabeling, brains were rinsed 3 times for 1 hour each with PTwH buffer, consisting of 1X PBS, 0.2% Tween-20, 10mg heparin, and 2g of NaN_3. For primary antibody incubations, antibodies were diluted in antibody solution consisting of PTwH buffer with 5% DMSO and 3% normal donkey serum. Antibodies to α-smooth muscle actin (α-SMA) (Rabbit anti- α-SMA, Abcam, cat: ab5694, dilution 1:1000) and transgelin (Sm22)(Rabbit anti-Sm22 Abcam; ab14106, dilution 1:1500) were combined to label the artery wall, as previously described.[18] Pan-vascular labeling was achieved through staining with DyLight-594 labeled Lycopersicon Esculentum (Tomato) Lectin (Vector labs, cat. no.: DL-1177-1), which was added to both primary and secondary incubations at 1:100 concentration. Pericytes were labeled by combining PDGFRβ (Goat anti-PDGFRβ, R&D Systems; AF1042, dilution: 1:100) and Mouse Aminopeptidase

N/CD13 (Goat anti-CD13, R&D Systems; AF2335, dilution: 1:100). Primary antibodies were incubated for 10 days at 37°C. Following primary incubation, PTwH buffer was changed 4-5 times for each sample over the course of 24 hours. A fresh antibody solution was used to dilute all secondary antibodies to a concentration of 1:500. For secondary antibodies, Alexa Fluor® 488-AffiniPure Fab Fragment Donkey Anti-Rabbit IgG (H+L) (Jackson ImmunoResearch laboratories; 711-547-003) was used to detect artery staining and Alexa Fluor® 647-AffiniPure Fab Fragment Donkey Anti-Goat IgG (H+L) (Jackson ImmunoResearch laboratories; 705-607-003) was utilized to detect pericyte staining. After secondary incubation for 10 days at 37°C, brains were washed 4-5 times in PTwH buffer for 24 hours. Brain samples were then dehydrated in a series of methanol dilutions in water (1-hour washes in 20%, 40%, 60%, 80% and 100%). An additional wash of 100% methanol was conducted overnight to remove any remaining water. The next day, brains were incubated in 66% dichloromethane/33% methanol for 3 hours and subsequently incubated in 100% dichloromethane twice for at least 15 minutes each. Brains were equilibrated in dibenzyl ether for at least two days before transitioning to ethyl cinnamate one day prior to imaging.

Light-sheet imaging. A SmartSPIM light-sheet fluorescence microscope (LifeCanvas Technologies) was used to image cleared and stained mouse brains. Brains were supported in the custom sample holder by standardized pieces of dehydrated agarose consisting of 1% agarose in 1X TAE buffer. The sample holder arm was then submerged in ethyl cinnamate for imaging. We used a 3.6X objective (LifeCanvas, 0.2 NA, 12 mm working distance, 1.8 μm lateral resolution) and three lasers (488nm, 560nm, 642nm wavelengths) with a 2 μm step size. Acquired data was stitched using custom Matlab codes adapted from Wobbly Stitcher.[18,54]

Analysis of light sheet imaging data. For the analysis of the abundance and penetration depth of cortical penetrating vessels, a 2 mm (x) by 2 mm (y) by 1.2 mm (z) ROI centered on the primary somatosensory cortex was cropped from whole brain light sheet data sets of 4 adult mice (**Extended Fig. 1c-e**). The pial penetration points of all penetrating vessels subtypes (penetrating arteriole, PCVs and other ascending venules) were identified within the ROI and the distance to vessel ending points within the tissue was recorded. For penetrating arterioles, we defined the ending point as the deepest region where α-SMA/Sm22 staining was still discernible. For ascending venules and PCVs, the ending point was defined as the region where the main trunk ended and ramified into many smaller branches, as visualized by lectin staining. PCVs were clearly distinguished from other ascending venules by their large diameter, weak α-SMA/Sm22

staining of the vessel wall and specific branching pattern in the white matter of the CC. Image cropping and analysis was performed using the Fiji software.

For the analysis of vascular length density and pericyte density across different cortical layers, a 540 μm (x) by 540 μm (y) by 1000 μm (z) ROI centered on the primary somatosensory cortex was cropped from whole brain light sheet data sets of 4 adult and 4 aged mice (**Fig. 8e, f**). The ROI volumes were then further divided into 200 μm thick (z) subsections (**Fig. 8g, h**). The 3D segmentation of all vessels labeled with lectin, as well as annotation of all capillary PDGFRβ+CD13 labeled pericytes was performed using the Filament Tracer module of Imaris software (**Fig. 8i, j**). Only mesh and thin strand pericytes on small diameter vessels, characterized by the "bump on the log" morphology, were included in the analysis. Vascular length density (total vascular length per mm^3) and pericyte density (total number of pericyte cell bodies) were measured for each subsection. Then the normalized pericyte density was calculated by dividing the pericyte and vascular length density values for each subsection.

In silico modeling of microvascular networks. Both microvascular networks used for *in silico* modeling in this work (MVN1 and MVN2) were acquired from the vibrissa primary sensory cortex of C57/BL6 male mice by Blinder et al.[55] In these segmented and vectorized networks, each vessel is represented by an edge with a given length and diameter, and edges are connected at bifurcations (graph vertices). MVN1 and MVN2 are embedded in a tissue volume of ~1.6 mm^3 and ~2.2 mm^3 and contain ~12,100 and ~19,300 vessels, respectively. The vessels are labeled as pial arteries, penetrating arterioles, capillaries, ascending venules, and pial veins. The predominant vascular length is composed of capillaries (96% and 94% of total vascular length in MVN1 and MVN2, respectively). As staining of mural cells is not available for the microvascular network reconstructions, the vessel identities are based on topology and diameter.[55]

Blood flow modeling with discrete RBC tracking. The numerical model to simulate blood flow with discrete red blood cell (RBC) tracking in realistic microvascular networks has been described in Schmid et al.[23] Below, we briefly summarize the key aspects of the modeling approach, which have been detailed in prior studies.[23,56] The modeling approach is based on the small Reynolds number (Re < 1.0 for all vessels) in the microvasculature. As such the flow is laminar and mostly even in the Stokes regime, which allows describing the flow in individual vessels by Poiseuille's law. The flow rate q_{ij} in vessel *ij* between node *i* and *j* is computed by:

$$q_{ij} = \frac{p_i - p_j}{R_{ij}^e} = \frac{\pi\, D_{ij}^4}{128\, L_{ij}\, \mu\, \mu_{rel}^e}\, (p_i - p_j)$$

where D_{ij} and L_{ij} are the vessel diameter and the length and p_i and p_j are the pressure at node i and j, respectively. μ is the dynamic plasma viscosity and μ_{rel}^{e} is the relative effective viscosity, which accounts for the presence of RBCs and is computed as a function of local hematocrit and vessel diameter as described in Pries et al. (*in vitro* formulation).[32]

To compute the local hematocrit, we track individual RBCs through the MVNs. Hereby, we need to account for the Fahraeus effect (RBC velocity is larger than bulk flow velocity) and the phase separation (RBCs partition with a different ratio than the bulk flow at divergent bifurcations).[32] At divergent bifurcations with a diameter >10 µm the phase separation is described by empirical equations.[32] At smaller diameters, RBCs transit in single file and consequently, the RBC motion can be approximated by assuming that the RBCs follow the path of the largest pressure force.[23,57] It is important to note that the RBC distribution and the flow field fluctuate in time and that the RBC distribution impacts the local flow field.[29,56] In this study, we use the time-averaged flow field to compare changes in response to cortical layer-specific alterations in capillary diameters. The time-averaged flow field is computed by averaging over 12-20s. The exact averaging interval depends on the vessel-specific turn-over time (vessel length/RBC velocity) and ensures that 90% of all vessels are perfused at least six times.

Two configurations were considered regarding the boundary conditions for in- and outflow vertices below the cortical surface. In configuration 1 ("*open*"), fixed pressure values are assigned at all in- and outflows. These values are kept constant for all scenarios mimicking vascular alterations during aging (see below). Further details on assigning suitable pressure boundary conditions can be found in our prior studies.[23] In configuration 2 ("*trimmed*") we assume that no blood flow enters/leaves the simulation domain below the cortical surface and that all flow enters/leaves via the pial vessels at the cortical surface. This approach is equivalent to assigning no-flow boundary conditions at in- and outflows below the cortical surface or to removing all in- and outflows below the cortical surface. Configuration 1 ("*open*") has the advantage that it does not underpredict perfusion, as is the case for trimmed networks.[58] On the other hand, the number of boundary nodes is significantly small for configuration 2 ("*trimmed*"). As such, this setup is less sensitive to the assigned boundary values, which is especially desirable for relatively large microvascular alterations. Thus, for the current study, we decided to consider both open and trimmed boundary conditions for a total of four configurations: MVN1-open, MVN1-trimmed, MVN2-open, and MVN2-trimmed. The inflow hematocrit of 0.3 is constant for all simulations.

Mimicking vascular alterations observed in aged mice in silico. We mimicked two age-related vascular alterations observed *in vivo* to understand their effects on microvascular perfusion: 1) vasoconstriction in capillaries of layer 6 (average diameter reduction of 7%) and 2) reduced capillary density in layer 6 (density reduction by 10%). Both vascular alterations occur in parallel, and we therefore studied the effect of each alteration individually and in a combined manner. As we are interested in perfusion changes with respect to cortical depth, each capillary is assigned to one of the five cortical layers (L1, L2/3, L4, L5, L6). This is done by computing the average depth per capillary from the tortuous vessel coordinates and assigning the capillary to the respective layer based on the minimum and maximum depth for each layer (L1: up to 200 µm, L2/3: 200-400 µm, L4: 400-600 µm, L5: 600-800 µm, L6: below 800 µm). Only capillaries within the 5th to 95th percentile of all vessel depths and at least two branches from any in-/outflow were considered for vasoconstriction and subsequent analyses. This is done to avoid confounding effects with respect to boundary conditions. For all configurations, the 95th percentile is at a depth of at least 999 µm and we have 8,000-14,000 capillaries for analyses.

To mimic vasoconstriction, all capillaries belonging to layer 6 are constricted by 7%. To reduce capillary density in layer 6, evidence from the current study suggests that shorter capillaries tend to regress more frequently during aging (**Supplementary Fig. 11**). Moreover, *in vivo* the focus is on pre-converging capillaries. These capillaries are positioned closer to the center of the capillary bed with respect to the total path from arteriole to venule. Consequently, we employ these two criteria to identify the subset of capillaries potentially affected by regression. The maximum length for a regressing capillary was set to 70 µm. The position of each capillary along the path from arteriole to venule was assigned a minimum distance to the penetrating arteriole trunk (*minDistMainDA*) and the ascending venule trunk (*minDistMainAV*). The 30th and the 10th percentile of all values for *minDistMainDA* and *minDistMainAV* set the threshold for defining the set of capillaries potentially affected by regression. These two criteria (length and position along the capillary path) yielded 191, 520, 1169, and 2088 capillaries potentially affected by regression in MVN1-open, MVN1-trimmed, MVN2-open, and MVN2-trimmed networks. Considering that the total number of capillaries in layer 6 is 1707, 1413, 4658, and 4925 for these networks, it implied that 170, 141, 465, and 492 capillaries needed to be removed to mimic a density reduction by 10%. For each network, there were more capillaries that fit our selection criterion than needed to be removed from the network. Therefore, for each network we generated 5 cases where candidate capillaries were randomly removed to match the target density reduction of 10%. These 5 cases were then used to compute the average change for a density reduction of 10% per configuration. This increased robustness of blood flow outcomes measured for each

network. Capillary regression is modeled by constricting the selected capillaries by 97%. By comparing the average flow rate in the regressed capillaries to all flow rates in the network, we confirmed that the average flow rate in the regressed capillaries is close to zero (<2.5th percentile), effectively removing these capillaries from the perfused network.

The time-averaged flow field was computed for all four configurations (MVN1-open, MVN1-trimmed, MVN2-open, and MVN2-trimmed) and three scenarios each: 1) capillary vasoconstriction in L6, 2) reduced capillary density in L6 and 3) vasoconstriction and density reduction in L6. Quantities of interest were the flow rate, the RBC velocity, the RBC flux, and the linear density. The flow rate was directly obtained from the pressure drop across the vessel and the effective flow resistance. The RBC velocity is computed by $vf \cdot q_{ij}/A_{ij}$, where A_{ij} is the vessel cross-section and vf is the velocity factor accounting for the increased velocity of RBCs in comparison to the bulk flow and which is defined as the ratio of discharge to tube hematocrit.[32] The discharge hematocrit is calculated in function of the tube hematocrit and the vessel diameter as defined in.[32] The RBC flux q_{ij}^{RBC} is the product of the flow rate q_{ij} and the discharge hematocrit htd divided by the RBC volume V^{RBC}, i.e., $q_{ij}^{RBC} = q_{ij} \cdot htd/V^{RBC}$. The RBC volume is 49 fl. As with the in vivo experiments, the linear density is computed by dividing the RBC flux by the RBC velocity.

In addition to comparing average perfusion quantities per layer (**Fig. 6c-e, Supplementary Fig. 12**), we computed the integral capillary inflow and outflow per cortical layer. Therefore, all startpoints and endpoints of the capillary bed were identified. A capillary start point is a bifurcation at which the vessel label changes from arterial vessel to capillary. The transition point between capillary and venule vessel marks a capillary endpoint. Capillary start and endpoints were assigned to the different layers based on their cortical depth. To obtain the integral capillary inflow per cortical layer all arterial inflows into all capillary start points of the respective layer are summed (**Fig. 6f**). The equivalent computation is performed on the venule side to compute the integral outflow of the capillary bed (**Fig. 6g**).

Statistics. All statistical analyses for *in vivo* and light-sheet data were performed with SPSS software. Analysis of all parameters was performed using a repeated-measures analysis of variance (ANOVA) model or a linear mixed-effects model, with Age (adult vs. aged) and Layer (2/3 vs. 4 vs. 6/CC) set as independent factors, and Animal as a within group factor. Therefore, data from each animal was assigned to the corresponding age group, and further subdivided into the 3 analyzed layers. This strategy considers the nested nature of the data; that is, that multiple

vessels come from one animal and are thus not independent of one another. Strength and significance of correlation between analyzed parameters was determined using the Pearson correlation analysis in the GraphPad Prism version 9 software. All graphs were made using the GraphPad Prism version 9 software.

Animal and data exclusion criteria. Out of 12 adult chronic cranial windows, 1 got damaged before the line scan data for layer 6/CC could be obtained. Out of 12 aged windows 1 got damaged before the line scan data for layer 6/CC could be obtained, while for another only the line scan data for layer 6/CC was obtained. This resulted in 12 complete data sets for layers 2/3 and 4, and 11 complete data sets for layer 6/CC in the adult group, as well as 11 complete data sets for all layers in the aged group.

For analysis of structural and functional parameters of vascular segments, if the signal quality did not allow for reliable analysis of lumen diameter, RBC flux or blood flow velocity these parameters were excluded from the analysis for the corresponding vessel segment, while the length and tortuosity data were included. Correlation analyses were performed only on the population of vessels where all analyzed structural and functional parameters could be obtained.

ACKNOWLEDGMENTS. This work was supported by grants from the NIH/NIA (R01AG062738, R21AG069375, RF1AG077731, R01AG081840) and a pilot award from the Albert White Matter Institute. FS received funding from the Swiss National Science Foundation (Grant No. 202192). SKB was supported by fellowships from the NIH/NINDS (F32NS117649) and NIH/NIA (K99AG080034). MJS was supported by a Diversity supplement for a grant from the NIH/NIA (R01AG062738-03S1). We also thank Tiago Figueiredo for creating the artwork used in Fig. 2e,f. We would also like to thank Juliane Gust, Gokce Gurler and Catherine Foster for their helpful comments and suggestions during manuscript preparation.

REFERENCES:

1 Gunning-Dixon, F. M., Brickman, A. M., Cheng, J. C. & Alexopoulos, G. S. Aging of cerebral white matter: a review of MRI findings. *Internation Journal of Geriatric Psychiatry* **24**, 109-117 (2009).

2 Gorelick, P. B. *et al.* Vascular contributions to cognitive impairment and dementia: A statement for healthcare professionals from the American Heart Association/American Stroke Association. *Stroke* **42**, 2672-2713 (2011).

3 Wardlaw, J. M., Smith, C. & Dichgans, M. Small vessel disease: mechanisms and clinical implications. *Lancet Neurology* **18**, 684-696 (2019).

4 Iturria-Medina, Y. *et al.* Early role of vascular dysregulation on late-onset Alzheimer's disease based on multifactorial data-driven analysis. *Nature Communications* **7**, 11934 (2016).
5 Bouvy, W. H. *et al.* Abnormalities of Cerebral Deep Medullary Veins on 7 Tesla MRI in Amnestic Mild Cognitive Impairment and Early Alzheimer's Disease: A Pilot Study. *Journal of Alzheimer's Disease* **57**, 705-710 (2017).
6 Keith, J. *et al.* Collagenosis of the Deep Medullary Veins: An Underrecognized Pathologic Correlate of White Matter Hyperintensities and Periventricular Infarction? *Journal of neuropathology and experimental neurology* **76**, 299-312 (2017).
7 Phillips, O. R. *et al.* The superficial white matter in Alzheimer's disease. *Human brain mapping* **37**, 1321-1334 (2016).
8 Reginold, W. *et al.* Altered Superficial White Matter on Tractography MRI in Alzheimer's Disease. *Dementia and geriatric cognitive disorders extra* **6**, 233-241 (2016).
9 Duvernoy, H. M., Delon, S. & L., V. J. Cortical blood vessels of the human brain. *Brain Research Bulletin* **7**, 519-579 (1981).
10 Koizumi, K. *et al.* Apoε4 disrupts neurovascular regulation and undermines white matter integrity and cognitive function. *Nature Communications* **9**, 3816 (2018).
11 Lai, A. Y. *et al.* Venular degeneration leads to vascular dysfunction in a transgenic model of Alzheimer's disease. *Brain* **138**, 1046-1058 (2015).
12 Salat, D. H. Imaging small vessel-associated white matter changes in aging. *Neuroscience* **276**, 174-186 (2014).
13 Brickman, A. M. *et al.* Reduction in cerebral blood flow in areas appearing as white matter hyperintensities on magnetic resonance imaging. *Psychiatry research* **172**, 117-120 (2009).
14 Chen, J. J., Rosas, H. D. & Salat, D. H. The relationship between cortical blood flow and sub-cortical white-matter health across the adult age span. *PLoS One* **8**, e56733 (2013).
15 Liu, H. *et al.* Aging of cerebral white matter. *Ageing Research Reviews* **34**, 64-76 (2017).
16 Murugesan, N., Demarest, T. G., Madri, J. A. & Pachter, J. S. Brain regional angiogenic potential at the neurovascular unit during normal aging. *Neurobiology of Aging* **33**, e1-16 (2012).
17 Schager, B. & Brown, C. E. Susceptibility to capillary plugging can predict brain region specific vessel loss with aging. *Journal of Cerebral Blood Flow & Metabolism* **40**, 2475-2490 (2020).
18 Bennett, H. C. *et al.* Aging drives cerebrovascular network remodeling and functional changes in the mouse brain. *bioRxiv* **05.23**, 541998 (2023).
19 Li, B. *et al.* Two-photon microscopic imaging of capillary red blood cell flux in mouse brain reveals vulnerability of cerebral white matter to hypoperfusion. *Journal of Cerebral Blood Flow & Metabolism* **40**, 501-512 (2019).
20 Horton, N. G. *et al.* In vivo three-photon microscopy of subcortical structures within an intact mouse brain. *Nature Photonics* **7**, 10.1038/nphoton.2012.1336. (2013).
21 Stamenkovic, S., Li, Y., Waters, J. & Shih, A. Deep imaging to dissect microvascular contributions to white matter degeneration in rodent models of dementia. *Stroke* **54**, 1403-1415 (2023).
22 Bennett, H. C. & Kim, Y. Advances in studying whole mouse brain vasculature using high-resolution 3D light microscopy imaging. *Neurophotonics* **9**, 021902 (2022).
23 Schmid, F., Tsai, P. S., Kleinfeld, D., Jenny, P. & Weber, B. Depth-dependent flow and pressure characteristics in cortical microvascular networks. *PloS Computational Biology* **13**, e1005392 (2017).
24 Hartmann, D. A. *et al.* Brain capillary pericytes exert a substantial but slow influence on blood flow. *Nature neuroscience* **24**, 633-645 (2021).

25 Santisakultarm, T. P. *et al.* In vivo two-photon excited fluorescence microscopy reveals cardiac- and respiration-dependent pulsatile blood flow in cortical blood vessels in mice. *American Journal of Physiology: Heart and Circulatory Physiology* **302**, H1367-H1377 (2012).
26 Cruz Hernández, J. C. *et al.* Neutrophil adhesion in brain capillaries reduces cortical blood flow and impairs memory function in Alzheimer's disease mouse models. *Nature Neuroscience* **22**, 413-420 (2019).
27 Reeson, P., Choi, K. & Brown, C. E. VEGF signaling regulates the fate of obstructed capillaries in mouse cortex. *Elife* **7** (2018).
28 Secomb, T. W. Red blood cell mechanics and capillary blood rheology. *Cell Biophysics* **18**, 231-251 (1991).
29 Schmid, F., Barrett, M. J. P., Obrist, D., Weber, B. & Jenny, P. Red blood cells stabilize flow in brain microvascular networks. *PloS Computational Biology* **15**, e1007231 (2019).
30 Cai, C. *et al.* Impaired dynamics of precapillary sphincters and pericytes at first-order capillaries predict reduced neurovascular function in the aging mouse brain. *Nature Aging* **3**, 173-184 (2023).
31 Gao, Y. R. *et al.* Time to wake up: Studying neurovascular coupling and brain-wide circuit function in the un-anesthetized animal. *Neuroimage* **153**, 382-398 (2017).
32 Pries, A. R. & Secomb, T. W. Microvascular blood viscosity *in vivo* and the endothelial surface layer. *American Journal of Physiology - Heart and Circulation Physiology* **289**, H2657-2664 (2005).
33 Nortley, R. *et al.* Amyloid β oligomers constrict human capillaries in Alzheimer's disease via signaling to pericytes. *Science* **365**, Epub 2019 Jun 2020 (2019).
34 Berthiaume, A. A. *et al.* Pericyte remodeling is deficient in the aged brain and contributes to impaired capillary flow and structure. *Nature Communications* **13**, 5912 (2022).
35 Montagne, A. *et al.* Pericyte degeneration causes white matter dysfunction in the mouse central nervous system. *Nature Medicine* **24**, 326-337 (2018).
36 Choe, Y. G. *et al.* Pericyte Loss Leads to Capillary Stalling Through Increased Leukocyte-Endothelial Cell Interaction in the Brain. *Frontiers in Cellular Neuroscience* **16**, 848764 (2022).
37 Li, Y. *et al.* Aging-associated changes in cerebral vasculature and blood flow as determined by quantitative optical coherence tomography angiography. *Neurobiology of Aging* **70**, 148-159 (2018).
38 Brown, W. R. & Thore, C. R. Cerebral microvascular pathology in aging and neurodegeneration. *Neuropathology and applied neurobiology* **37**, 56-74 (2011).
39 Desjardins, M., Berti, R., Lefebvre, J., Dubeau, S. & Lesage, F. Aging-related differences in cerebral capillary blood flow in anesthetized rats. *Neurobiology of Aging* **35**, 1947-1955 (2014).
40 Shin, P. *et al.* Aerobic exercise reverses aging-induced depth-dependent decline in cerebral microcirculation. *Elife* **12**, e86329 (2023).
41 Li, B. *et al.* More homogeneous capillary flow and oxygenation in deeper cortical layers correlate with increased oxygen extraction. *Elife* **8**, e42299 (2019).
42 Moeini, M. *et al.* Compromised microvascular oxygen delivery increases brain tissue vulnerability with age. *Scientific Reports* **8**, 8219 (2018).
43 Raj, D. *et al.* Increased white matter inflammation in aging- and Alzheimer's disease brain. *Frontiers in Molecular Neuroscience* **10**, 206 (2017).
44 Soto, I. *et al.* APOE Stabilization by Exercise Prevents Aging Neurovascular Dysfunction and Complement Induction. *Plos Biology* **13**, e1002279 (2015).
45 Kisler, K. *et al.* Pericyte degeneration leads to neurovascular uncoupling and limits oxygen supply to brain. *Nature Neuroscience* **20**, 406-416 (2017).

46 Nikolakopoulou, A. M. *et al.* Pericyte loss leads to circulatory failure and pleiotrophin depletion causing neuron loss. *Nature Neuroscience* **22**, 1089-1098 (2019).
47 Hartmann, D. A., Coelho-Santos, V. & Shih, A. Y. Pericyte control of blood flow across microvascular zones in the central nervous system. *Annual Review of Physiology* **84**, 331-354 (2021).
48 Sargent, S. M. *et al.* Endothelial structure contributes to heterogeneity in brain capillary diameter. *Vascular Biology* **5**, e230010 (2023).
49 Shrouder, J. J. *et al.* Continued dysfunction of capillary pericytes promotes no-reflow after experimental stroke in vivo. *Brain* **Online ahead of print** (2023).

METHODS REFERENCES:

50 Preibisch, S., Saalfeld, S. & Tomancak, P. Globally optimal stitching of tiled 3D microscopic image acquisitions. *Bioinformatics* **25**, 1463-1465 (2009).
51 McDowell, K. P., Berthiaume, A. A., Tieu, T., Hartmann, D. A. & Shih, A. Y. VasoMetrics: Unbiased Spatiotemporal Analysis of Microvascular Diameter in Multi-photon Imaging Applications. *Quantitative Imaging in Medicine and Surgery* **11**, 969-982 (2021).
52 Kim, T. N. *et al.* Line-scanning particle image velocimetry: An optical approach for quantifying a wide range of blood flow speeds in live animals. *Public Library of Science ONE* **P7**, e38590 (2012).
53 Ouzounov, D. G. *et al.* In vivo three-photon imaging of activity of GCaMP6-labeled neurons deep in intact mouse brain. *Nature Methods* **14**, 388-390 (2017).
54 Kirst, C. *et al.* Mapping the Fine-Scale Organization and Plasticity of the Brain Vasculature. *Cell* **180**, 780-795 (2020).
55 Blinder, P. *et al.* The cortical angiome: An interconnected vascular network with noncolumnar patterns of blood flow. *Nature Neuroscience* **16**, 889-897 (2013).
56 Schmid, F., Reichold, J., Weber, B. & Jenny, P. The impact of capillary dilation on the distribution of red blood cells in artificial networks. *American Journal of Physiology: Heart and Circulatory Physiology* **308**, H733-H742 (2015).
57 Fung, Y. C. Stochastic flow in capillary blood vessels. *Microvascular Research* **5**, 34-48 (1973).
58 Lorthois, S., Cassot, F. & Lauwers, F. Simulation study of brain blood flow regulation by intra-cortical arterioles in an anatomically accurate large human vascular network. Part II: flow variations induced by global or localized modifications of arteriolar diameters. *Neuroimage* **54**, 2840–2853 (2011).

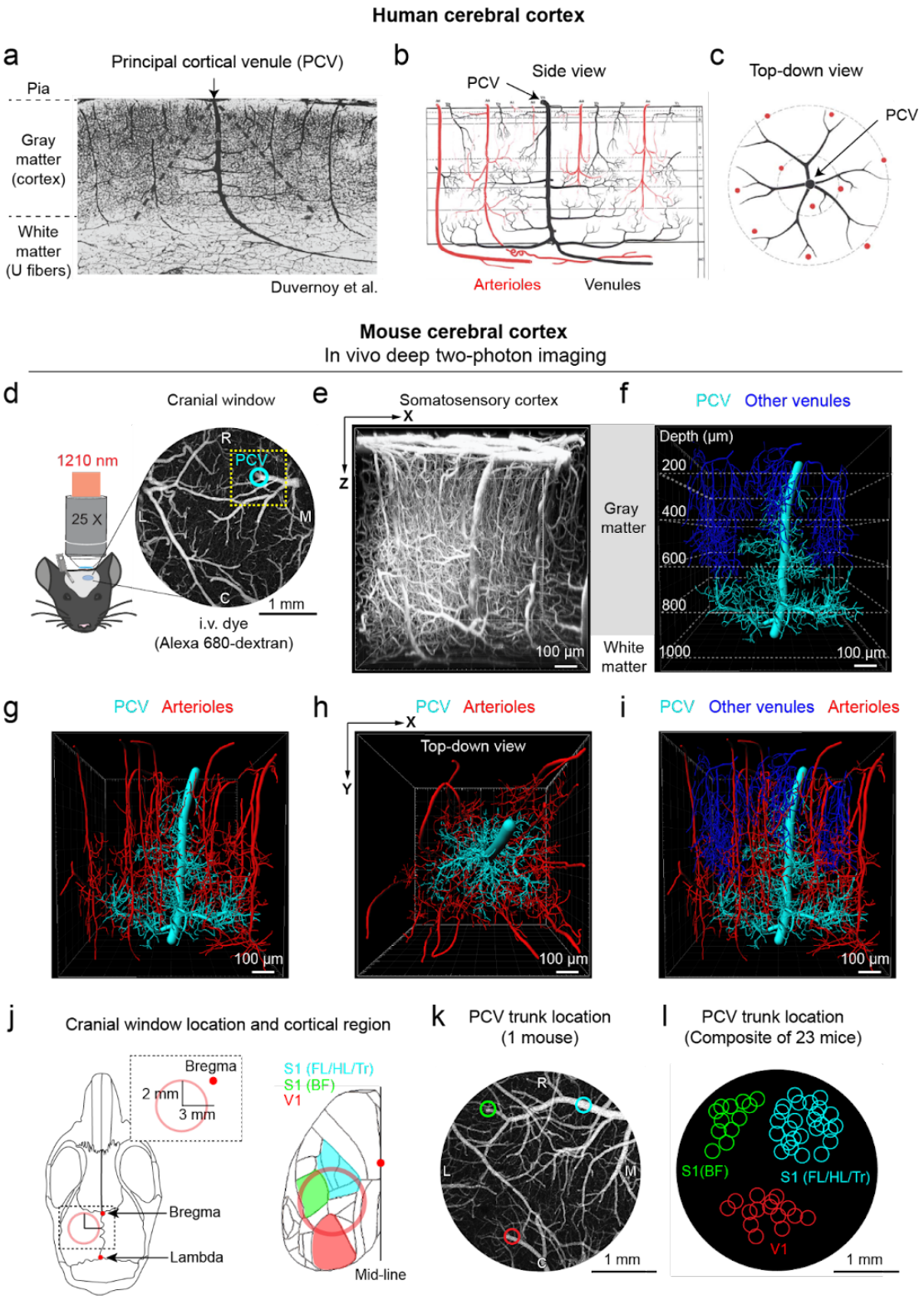

Figure 1. Principal cortical venules in human and murine brain. a. PCV visualized in India ink-filled human brain sections from Duvernoy et al.[9] **b, c.** Schematics from Duvernoy et al. show PCV structure from side (b) and above (c). **d.** Schematic summary of *in vivo* multi-photon imaging set up. The circular inset on the right shows an example low magnification image of the pial surface with PCV location marked with a cyan circle. **e.** Side view of the microvasculature in adult mouse somatosensory cortex within a 900 x 900 x 1000 µm (x, y, z) volume collected by deep two-photon imaging in panel d (field of view marked with the yellow square). **f.** Imaris reconstruction of a PCV together with branching networks (cyan). All other ascending venules (blue) are also depicted. Dotted lines mark the depth below the pial surface. **g, h.** PCV alongside all penetrating arterioles (red), viewed from side (f) and top (g). **I.** Composite of all segmented vessel types. **j.** Schematic of the mouse skull with calverial landmarks and bones labeled. The red circle marks the location of the implanted cranial windows and cortical sensory regions accessible within the window are shown on the right. S1 (FL/HL/Tr) – Somatosensory cortex forelimb, hindlimb, and trunk regions, S1 (BF) – Somatosensory cortex barrel field region, V1 – Primary visual cortex. **k.** PVC trunk locations within an example cranial window. **l.** The position of PCV trunk locations identified within cranial windows for n=23 mice, all verified by in vivo imaging. Cyan colored circles mark the locations of PCVs analyzed in this study.

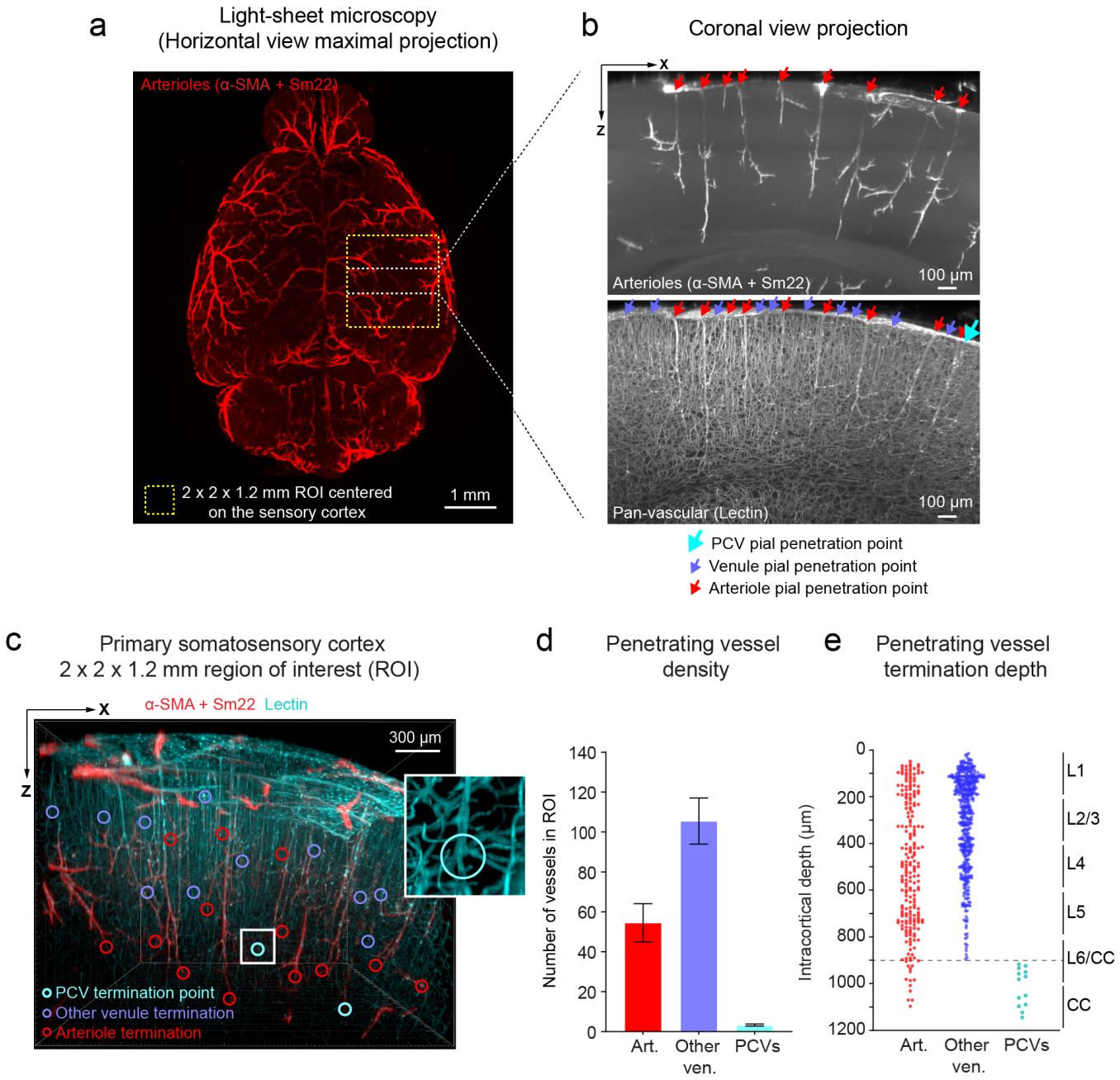

Extended Figure 1. Principal cortical venules in relation to other penetrating vessel types in the mouse brain. a. Light-sheet imaging data showing dorsal view of a mouse brain with arterioles labeled (Acta-2 and Sm22). The dotted yellow square marks the region of interest (ROI), centered on the primary somatosensory cortex, used for analysis of the number and penetration depths of cortical penetrating vessels. **b.** Maximum projection images showing the side view of the ROI defined by the white dotted lines in panel a, showing labeling of cortical arterioles by Acta-2 and Sm22 (upper panel) and all blood vessels by lectin (lower panel). Pial penetration points of arterioles and venules are marked with arrows. **c.** Side projection of analyzed volume with colored circles marking the intracortical termination points of different penetrating vessel types. The inset on the right shows an enlarged volume denoted by a white square, with a venule termination point marked by a cyan circle. **d.** Plot of the average number of penetrating vessel types within the ROIs. Data shown as mean ± SEM. (N = 4 adult mice). **e.** Plot of the intracortical termination depth of different penetrating vessel types. Each dot corresponds to a single vessel. Gray dotted line shows approximate depth of gray-white matter transition. Data shown as mean ± SEM. (N = 4 adult mice).

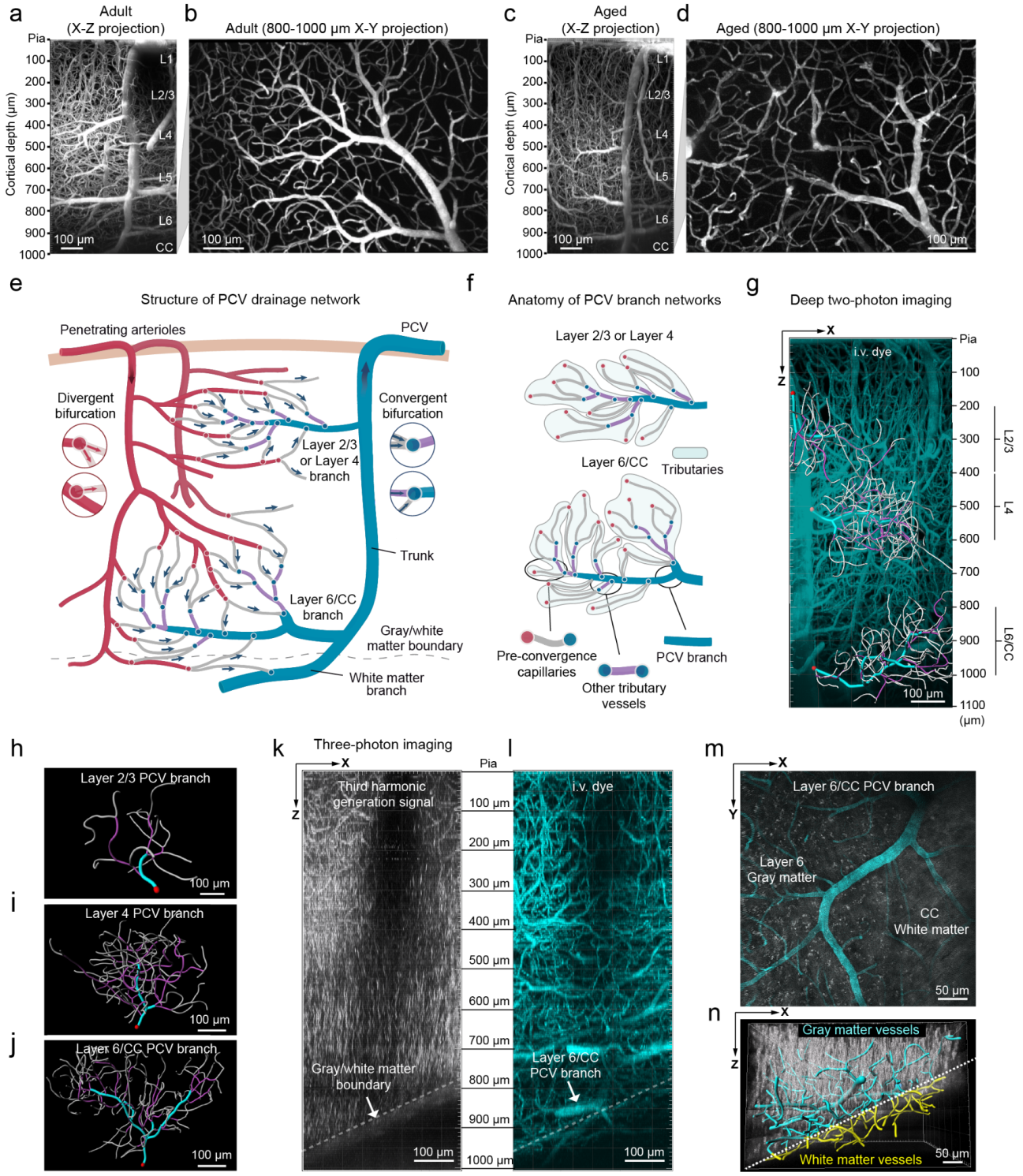

Figure 2. Structure and intracortical position of analyzed vascular networks of PCV branches. a-d. Maximum projection images of deep two-photon image stacks showing PCVs in a 6 months old adult mouse (a,b), and a 22 months old age mouse (c,d). **e,f.** Schematic of vessel types and their nomenclature in PCV networks. **g.** Side projection of *in vivo* deep two-photon image stack showing a PCV in an adult mouse, overlayed with Imaris reconstructions of PCV branch vascular networks in layers 2/3, 4 and 6. **h-j.** Top-down views of Imaris reconstructions of PCV branch vascular networks in layers 2/3, 4 and 6, respectively. Red circles correspond to the point where the main branch joins the main trunk of the PCV. The gray-colored vessels correspond to pre-convergence capillaries, violet-colored vessels represent other tributary vessels, while the cyan-colored segments correspond to the main branch segments. **k, l.** Three-photon imaging of PCV branches concurrent with 3HG signal to define the gray-white matter boundary. Side projections of three-photon image stacks showing the 3HG signal fluorescence from myelin (k) and the vasculature labeled with the FITC-dextran i.v. dye (l) in an awake adult mouse (6 months old). The transition from gray to white matter is visible in the 3HG signal image (white dotted line). **m.** Maximum projection image showing a top-down view of the Layer 6/CC branch (750-1000 µm depth) from panel l. The white matter appears as a striated 3HG signal coming from axon bundles of the CC. **n.** Side view of Imaris reconstruction of the PCV branch in panel m. Vascular segments draining Layer 6 and the CC are labeled in cyan and yellow, respectively. The dotted white line marks the location of the gray/white matter transition.

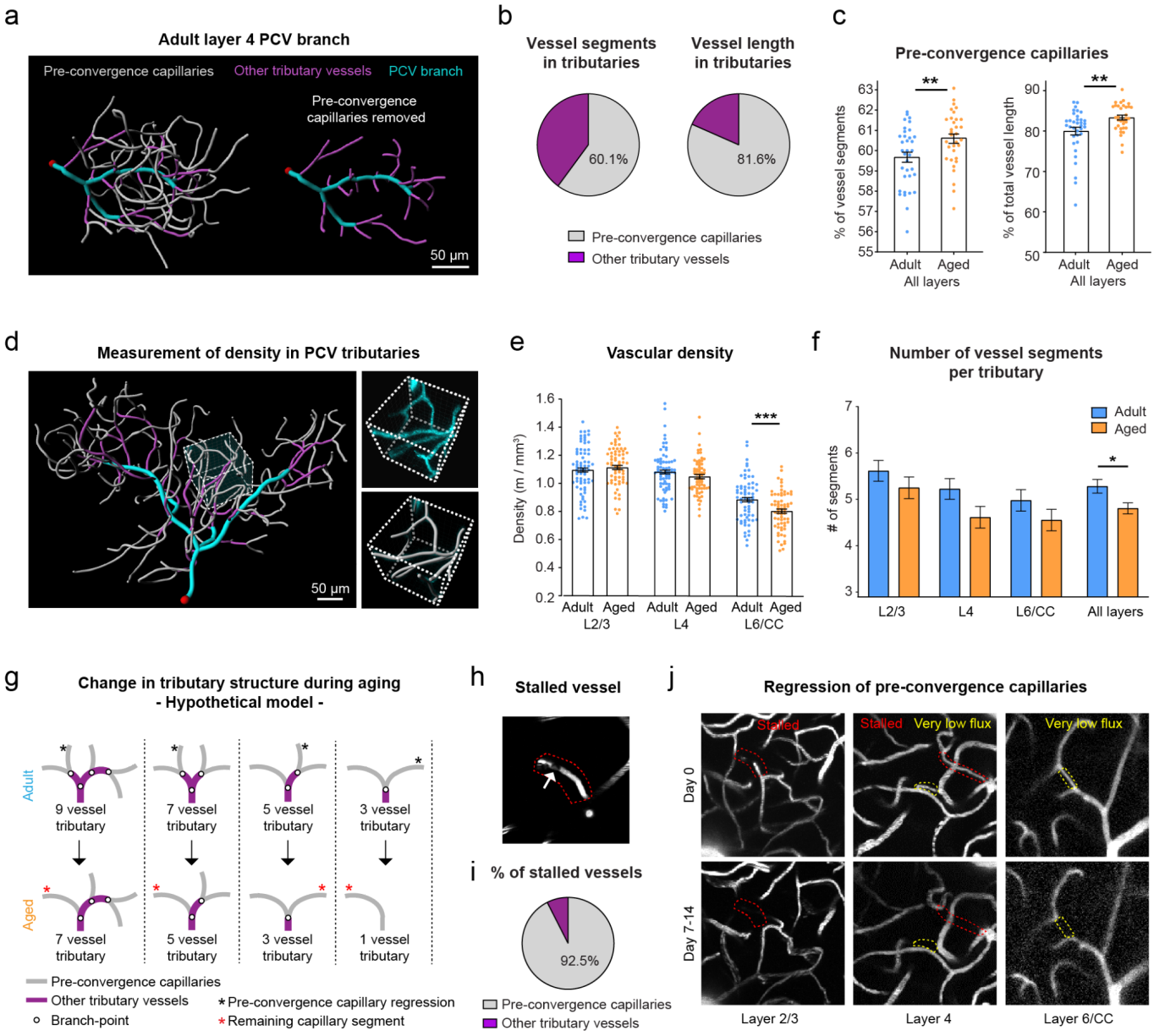

Figure 3. Reduced vascular density and simplified tributary PCV networks in aged mice. a. Images showing IMARIS reconstruction of an adult Layer 4 PCV vascular network with (left panel) and without (right panel) pre-convergence capillaries. **b.** Pie charts of the percentage (left) and length percentage (right) of pre-convergence capillaries and other tributary vessels in PCV vascular vessels (all analyzed layers and age groups pooled together). **c.** Percent of total vessel segments and vessel length corresponding to pre-convergence capillaries in PCV vascular networks in adult and aged mice (see Supplementary Fig. 3a,b for analysis of all layers and statistical details). **d.** Imaris reconstruction of an adult Layer 6/CC PCV vascular network showing 1 of 6 analyzed ROIs, targeting tributary vessels, for vascular length density measurements. Inset shows raw data and segmented vessels in an ROI. **e.** Vascular length density in PCV vascular networks of adult and aged mice across cortical layers. Two-way ANOVA analysis with Holm-Sidak's post-hoc comparison testing, Age group $F(1,340)=8.679$; $p=0.003$. Layer 2/3, $p=0.401$. Layer 4, $p=0.119$. Layer 6/CC, $p<0.001$. Adult, n=12 mice for layer 2/3 and layer 4, and 11 mice for layer 6/CC; Aged, n=11 mice for all layers. Data shown as mean ± SEM. **f.** Average number of vascular segments in tributaries of adult and aged mice across analyzed cortical layers. Two-way ANOVA analysis with Holm-Sidak's post-hoc comparison testing, Age group $F(1,62)=6.186$; $p=0.016$. Layer 2/3, $p=0.264$. Layer 4, $p=0.063$. Layer 6/CC, $p=0.202$. Adult, n=12 mice for layer 2/3 and layer 4, and 11 mice for layer 6/CC; Aged, n=11 mice for all layers. Data shown as mean ± SEM. **g.** Schematic showing a hypothetical model to explain change in tributary complexity of aged mice involving pre-convergence capillary regression (marked with a gray asterisk). **h.** Example of a stalled blood flow in pre-convergence capillary observed during *in vivo* deep two-photon imaging (marked with dotted red lines). The shadow of the cell responsible for capillary plugging can be seen (marked with white arrow). **i.** Pie chart showing vessel types experiencing stalled flow (all analyzed layers and age groups pooled together). **j.** Examples of pre-convergence capillaries in adult mice exhibiting very low (yellow dotted lines) or stalled (red dotted lines) blood flow (upper row images) that regressed over time (bottom row images).

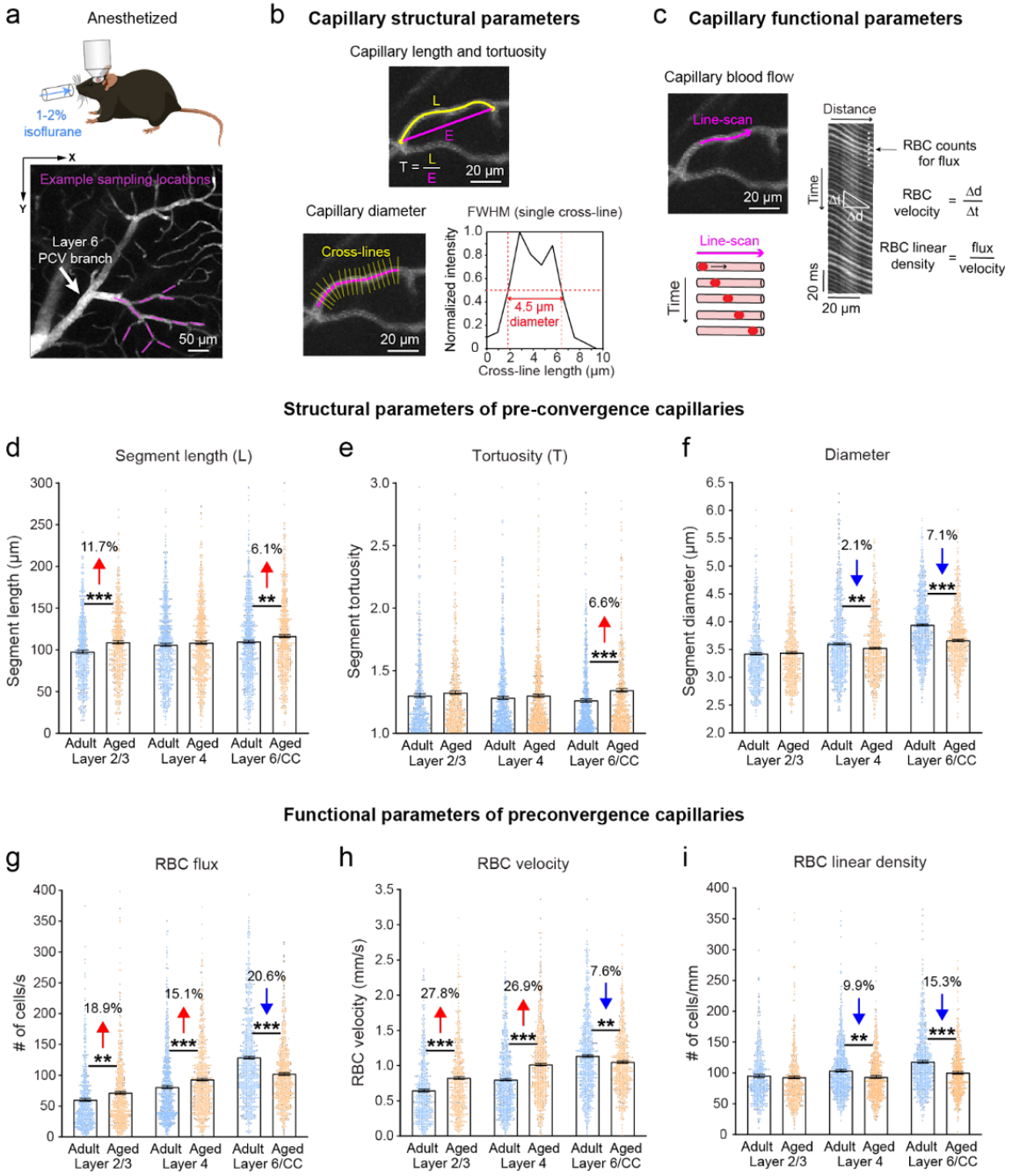

Figure 4. Age-related changes in pre-convergence capillaries under isoflurane anesthesia. a. Schematic showing a mouse imaged under isoflurane anesthesia and an example L6/CC vascular network with locations of data sampling (purple lines). **b.** Measurement of structural properties of pre-convergence capillaries, including capillary segment length (L) and tortuosity (T), which is L divided by the euclidean distance (E) between the branch points at either end of the vascular segment. Capillary diameter was assessed using VasoMetrics (see Material and Methods). **c.** Acquisition of line-scans enables tracking of RBC shadows over time, which is used to calculate RBC flux by counting of cell shadows and RBC velocity by automated calculation of the slope of the RBC shadows (see Material and Methods). Linear density is calculated as RBC flux divided by RBC velocity. **d.** Length of pre-convergence capillaries across different cortical layers and age groups. Two-way ANOVA analysis with Holm-Sidak's post-hoc comparison testing, Age group $F(1,4127)=22.481$; $p<0.001$; Layer 2/3, $p<0.001$; Layer 4, $p=0.305$; Layer 6/CC, $p=0.007$. **e.** Tortuosity of pre-convergence capillaries across different cortical layers and age groups. Two-way ANOVA analysis with Holm-Sidak's post-hoc comparison testing, Age group $F(1,4127)=12.924$; $p<0.001$; Layer 2/3, $p=0.267$; Layer 4, $p=0.351$; Layer 6/CC, $p<0.001$. **f.** Diameter of pre-convergence capillaries across different cortical layers and age groups. Two-way ANOVA analysis with Holm-Sidak's post-hoc comparison testing, Age group $F(1,4147)=39.630$; $p<0.001$; Layer 2/3, $p=0.565$; Layer 4, $p=0.006$; Layer 6/CC, $p<0.001$. **g.** RBC flux in pre-convergence capillaries across different cortical layers and age groups. Two-way ANOVA analysis with Holm-Sidak's post-hoc comparison testing, Age group x Layer interaction $F(2,4056)=48.065$; $p<0.001$; Layer 2/3, $p=0.001$; Layer 4, $p<0.001$; Layer 6/CC, $p<0.001$. **h.** RBC velocity in pre-convergence capillaries across different cortical layers and age groups. Two-way ANOVA analysis with Holm-Sidak's post-hoc comparison testing, Age group $F(1, 4053)=55.672$; $p<0.001$; Layer 2/3, $p<0.001$; Layer 4, $p<0.001$; Layer 6/CC, $p=0.001$. **i.** RBC linear density in pre-convergence capillaries across different cortical layers and age groups. Two-way ANOVA analysis with Holm-Sidak's post-hoc comparison testing, Age group $F(1,4043)=24.804$; $p<0.001$; Layer 2/3, $p=0.499$; Layer 4, $p=0.002$; Layer 6/CC, $p<0.001$. For all plots, the Adult group includes n=12 mice for layers 2/3 and 4, and 11 mice for layer 6/CC; the Aged group includes n=11 mice for all layers. Data shown as mean ± SEM. * denotes statistically significant differences between age groups.

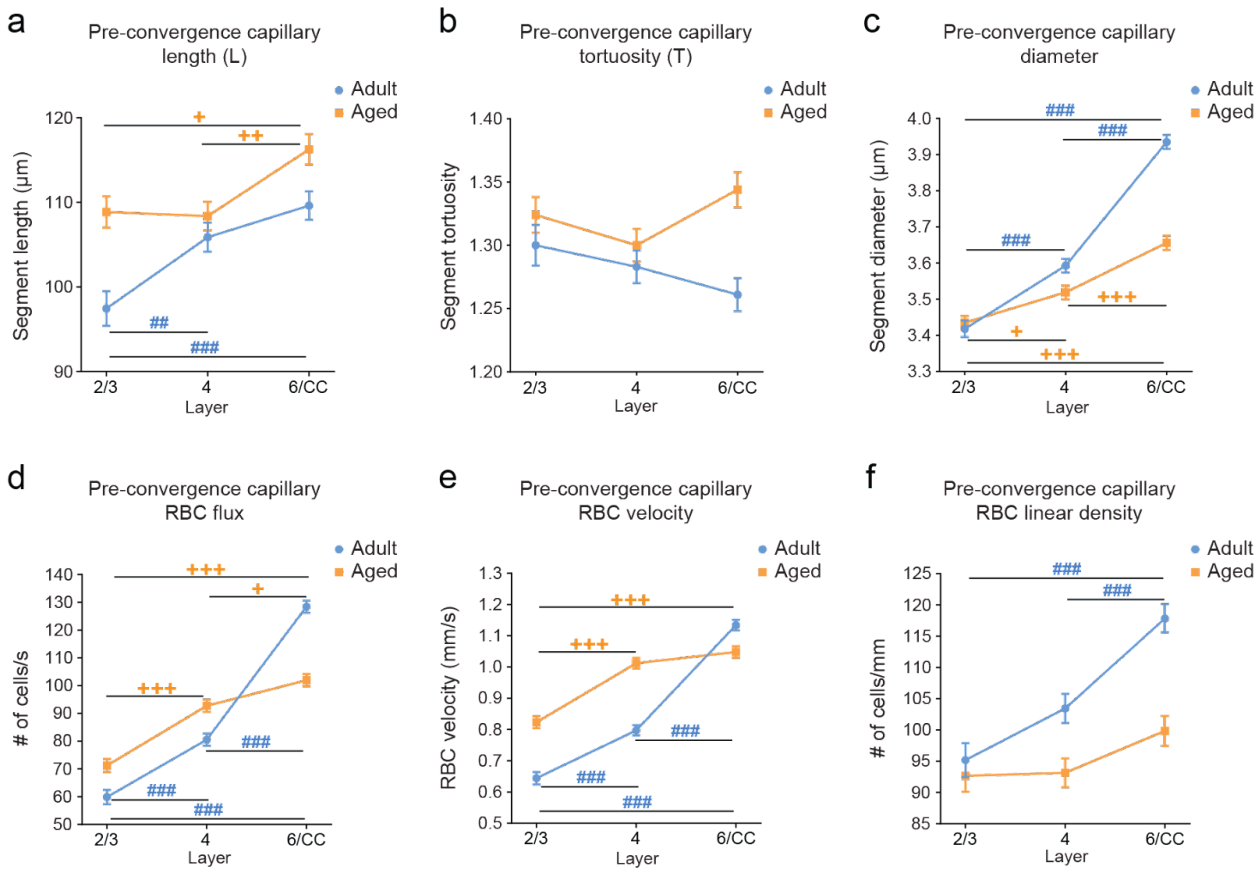

Extended Figure 2. Age and cortical layer-specific changes in pre-convergence capillaries under isoflurane anesthesia. a. Length of pre-convergence capillaries across different cortical layers within age groups. Two-way ANOVA analysis with Holm-Sidak's post-hoc comparison testing, Layer F(2,4127)=15.139; p<0.001. Adult, 2/3 vs. 4 p=0.005, 2/3 vs. 6/CC p<0.001, 4 vs. 6/CC p=0.323; Aged, 2/3 vs. 4 p=0.997, 2/3 vs. 6/CC p=0.012, 4 vs. 6/CC p=0.004. **b.** Tortuosity of pre-convergence capillaries across different cortical layers within age groups. Two-way ANOVA analysis with Holm-Sidak's post-hoc comparison testing, Layer F(2,4127)=1.073; p=0.342. Adult, 2/3 vs. 4 p=0.774, 2/3 vs. 6/CC p=0.148, 4 vs. 6/CC p=0.555; Aged, 2/3 vs. 4 p=0.528, 2/3 vs. 6/CC p=0.673, 4 vs. 6/CC p=0.061. **c.** Diameter of pre-convergence capillaries across different cortical layers within age groups. Two-way ANOVA analysis with Holm-Sidak's post-hoc comparison testing, Layer F(2,4147)=170.157; p<0.001. Adult, 2/3 vs. 4 p<0.001, 2/3 vs. 6/CC p<0.001, 4 vs. 6/CC p<0.001; Aged, 2/3 vs. 4 p=0.010, 2/3 vs. 6/CC p<0.001, 4 vs. 6/CC p<0.001. **d.** RBC flux in pre-convergence capillaries across different cortical layers within age groups. Two-way ANOVA analysis with Holm-Sidak's post-hoc comparison testing, Layer F(2,4056)=228.048; p<0.001. Adult, 2/3 vs. 4 p<0.001, 2/3 vs. 6/CC p<0.001, 4 vs. 6/CC p<0.001; Aged, 2/3 vs. 4 p<0.001, 2/3 vs. 6/CC p<0.001, 4 vs. 6/CC p=0.011. **e.** RBC velocity in pre-convergence capillaries across different cortical layers within age groups. Two-way ANOVA analysis with Holm-Sidak's post-hoc comparison testing, Layer F(2,4053)=191.197; p<0.001. Adult, 2/3 vs. 4 p<0.001, 2/3 vs. 6/CC p<0.001, 4 vs. 6/CC p<0.001; Aged, 2/3 vs. 4 p<0.001, 2/3 vs. 6/CC p<0.001, 4 vs. 6/CC p=0.394. **f.** RBC linear density in pre-convergence capillaries across different cortical layers within age groups. Two-way ANOVA analysis with Holm-Sidak's post-hoc comparison testing, Layer F(2,4043)=19.459; p<0.001. Adult, 2/3 vs. 4 p=0.061, 2/3 vs. 6/CC p<0.001, 4 vs. 6/CC p<0.001; Aged, 2/3 vs. 4 p=0.999, 2/3 vs. 6/CC p=0.115, 4 vs. 6/CC p=0.129. For all plots, the Adult group includes n=12 mice for layers 2/3 and 4, and 11 mice for layer 6/CC; the Aged group includes n=11 mice for all layers. Data shown as mean ± SEM. # denotes statistically significant differences between layers in adult mice, + denotes statistically significant differences between layers in aged mice.

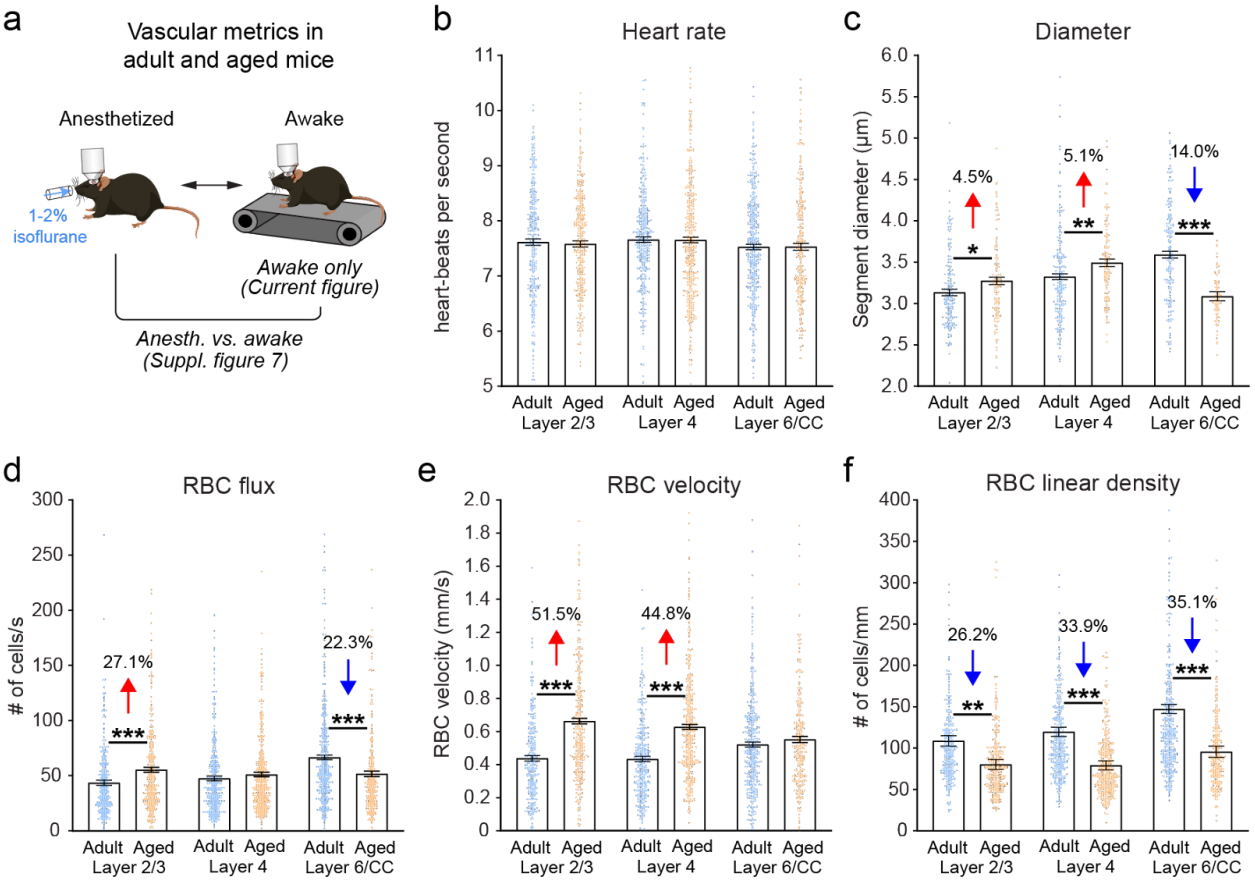

Figure 5. Age-related changes in pre-convergence capillaries in the awake state. a. Schematic depicting an imaging pipeline to capture the same PCV vascular networks in both the anesthetized state (isoflurane) and awake states over alternating imaging sessions. Vascular data from the awake state is shown in this figure and comparative anesthetized-awake data in Supplementary Fig. 7. **b.** Heart rate extracted from line-scans collected across different cortical layers and age groups. Two-way ANOVA analysis with Holm-Sidak's post-hoc comparison testing, Age group F(1,1958)=0.848; p=0.357; Layer 2/3, p=0.664; Layer 4, p=0.177; Layer 6/CC, p=0.960. **c.** Diameter of pre-convergence capillaries across different cortical layers and age groups. Two-way ANOVA analysis with Holm-Sidak's post-hoc comparison testing, Age group x Layer interaction F(2,859)=33.596; p<0.001; Layer 2/3, p=0.019; Layer 4, p=0.003; Layer 6/CC, p<0.001. **d.** RBC flux in pre-convergence capillaries across different cortical layers and age groups. Two-way ANOVA analysis with Holm-Sidak's post-hoc comparison testing, Age group F(2,1943)=20.674; p<0.001; Layer 2/3, p<0.001; Layer 4, p=0.227; Layer 6/CC, p<0.001. **e.** RBC velocity in pre-convergence capillaries across different cortical layers and age groups. Two-way ANOVA analysis with Holm-Sidak's post-hoc comparison testing, Age group F(1, 1942)=130.757; p<0.001; Layer 2/3, p<0.001; Layer 4, p<0.001; Layer 6/CC, p=0.198; **f.** RBC linear density in pre-convergence capillaries across different cortical layers and age groups. Two-way ANOVA analysis with Holm-Sidak's post-hoc comparison testing, Age group F(1,1928)=72.305; p<0.001; Layer 2/3, p=0.001; Layer 4, p<0.001; Layer 6/CC, p<0.001. For plots b, d, e and f, the Adult group includes n=5 mice for all layers; the Aged group includes n=6 mice for layer 2/3 and layer 4, and 5 mice for layer 6/CC. For plot c, the Adult group includes n=3 mice per layer; the Aged group includes n=2 mice per layer. Data shown as mean ± SEM. * denotes statistically significant differences between age groups.

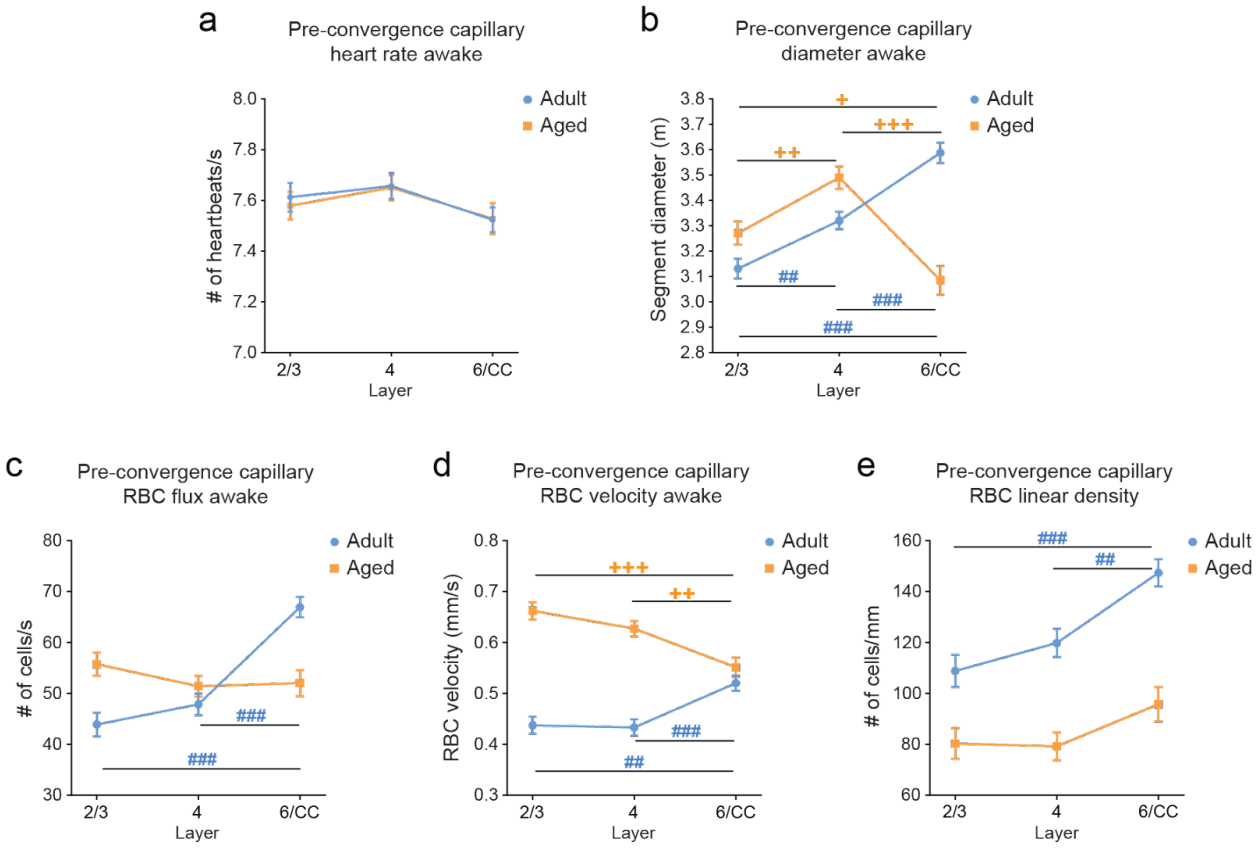

Extended Figure 3. Age and cortical layer-specific changes in pre-convergence capillaries in the awake state. a. Heart rate in pre-convergence capillary line scans across different cortical layers within age groups. Two-way ANOVA analysis with Holm-Sidak's post-hoc comparison testing, Layer F(2,1958)=1.223; p=0.295. Adult, 2/3 vs. 4 p=0.918, 2/3 vs. 6/CC p=0.552, 4 vs. 6/CC p=0.169; Aged, 2/3 vs. 4 p=0.993; 2/3 vs. 6/CC p=0.903; 4 vs. 6/CC p=0.967. **b.** Diameter of pre-convergence capillaries across different cortical layers within age groups. Two-way ANOVA analysis with Holm-Sidak's post-hoc comparison testing, Layer F(2,859)=12.374; p<0.001. Adult, 2/3 vs. 4 p=0.001, 2/3 vs. 6/CC p<0.001, 4 vs. 6/CC p<0.001; Aged, 2/3 vs. 4 p=0.002; 2/3 vs. 6/CC p=0.030; 4 vs. 6/CC p<0.001. **c.** RBC flux in pre-convergence capillaries across different cortical layers within age groups. Two-way ANOVA analysis with Holm-Sidak's post-hoc comparison testing, Layer F(2,1943)=11.643; p<0.001; Adult, 2/3 vs. 4 p=0.503, 2/3 vs. 6/CC p<0.001, 4 vs. 6/CC p<0.001; Aged, 2/3 vs. 4 p=0.398, 2/3 vs. 6/CC p=0.621, 4 vs 6/CC p=0.997. **d.** RBC velocity in pre-convergence capillaries across different cortical layers within age groups. Two-way ANOVA analysis with Holm-Sidak's post-hoc comparison testing, Layer F(2,1942)=1.189; p=0.305. Adult, 2/3 vs. 4 p=0.997, 2/3 vs. 6/CC p=0.001, 4 vs. 6/CC p<0.001; Aged, 2/3 vs. 4 p=0.325, 2/3 vs. 6/CC p<0.001, 4 vs. 6/CC p=0.006. **e.** RBC linear density in pre-convergence capillaries across different cortical layers within age groups. Two-way ANOVA analysis with Holm-Sidak's post-hoc comparison testing, Layer F(2,1928)=12.630; p<0.001. Adult, 2/3 vs 4 p=0.469, 2/3 vs 6/CC p<0.001, 4 vs 6/CC p=0.001; Aged, 2/3 vs 4 p=0.999, 2/3 vs 6/CC p=0.243, 4 vs 6/CC p=0.162. For plots a, c, d and e, the Adult group included n=5 mice for all layers; the Aged group included n=6 mice for layer 2/3 and layer 4, and 5 mice for layer 6/CC. For plot c, the Adult group includes n=3 mice per layer; the Aged group includes n=2 mice per layer. Data shown as mean ± SEM. # denotes statistically significant differences between layers in adult mice, + denotes statistically significant differences between layers in aged mice.

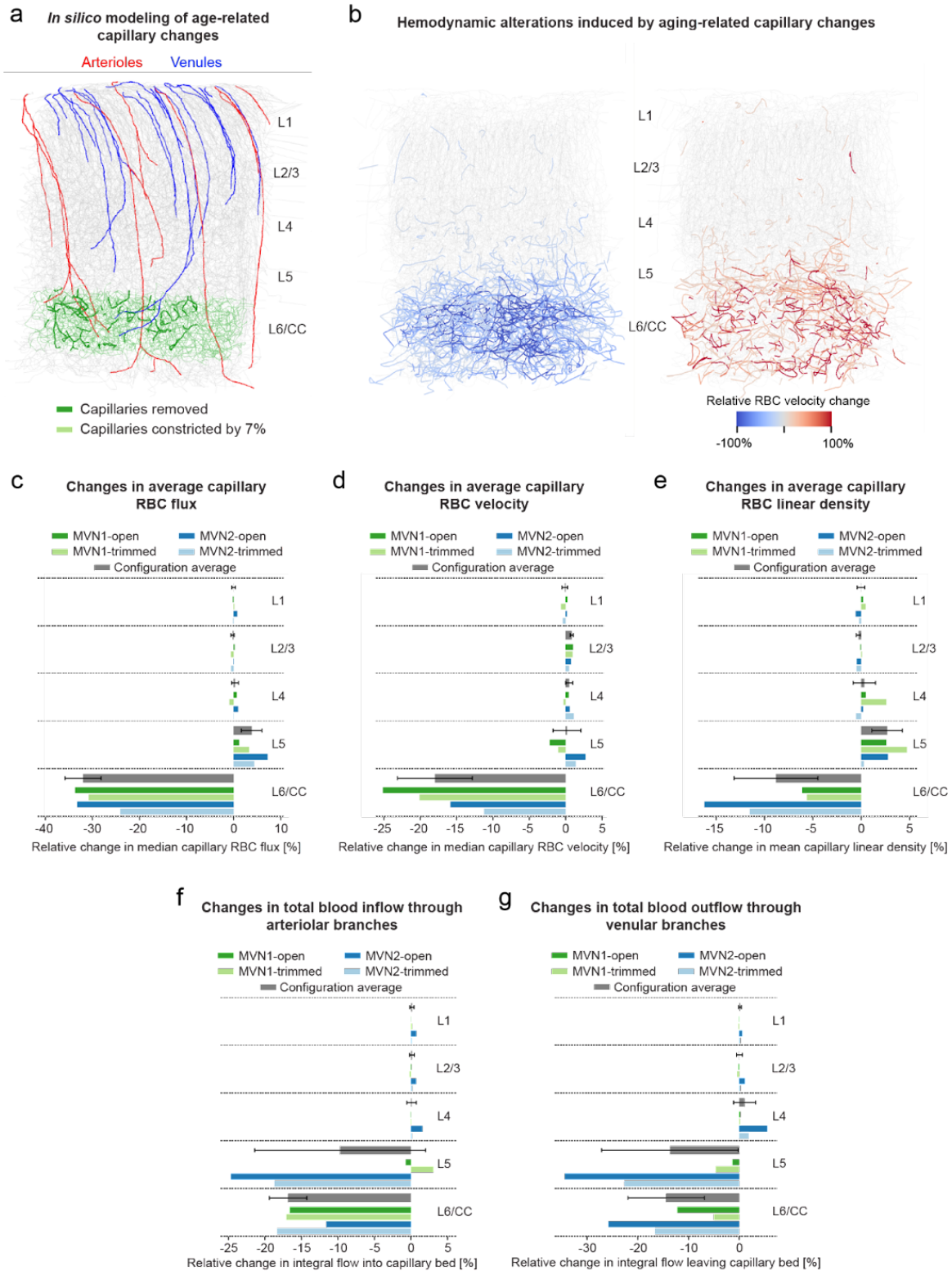

Figure 6. *In silico* modeling of age-related changes in capillary structure recapitulates blood flow deficit. a. Image of an *in silico* microvascular network with labeled penetrating arterioles (red) and ascending venules (blue). Age-related structural changes in layer 6/CC have been implemented in the model ("aged" microvascular network), including capillary constriction (light green segments) and removed segments to mimic capillary regression (dark green segments). **b.** Images of an "aged" *in silico* microvascular network with highlighted segments exhibiting reduced (left panel) or increased (right panel) RBC velocity. Only vessels with an absolute change larger than 10% are displayed. Panels a and b are MVN1-open configuration (see Methods) **c-e.** Changes in average capillary RBC flux (c), RBC velocity (d) and RBC linear density (e) across different cortical layers in "aged" *in silico* microvascular networks (N = 4 network configurations, 2 microvascular networks x 2 boundary conditions). Data shown as mean ± SD. **f, g.** Changes in total blood inflow into the capillary network through arteriolar branches (f), and total blood outflow through venular branches (g) across different cortical layers in "aged" *in silico* microvascular networks (N = 4 network configurations, 2 microvascular networks x 2 boundary conditions).

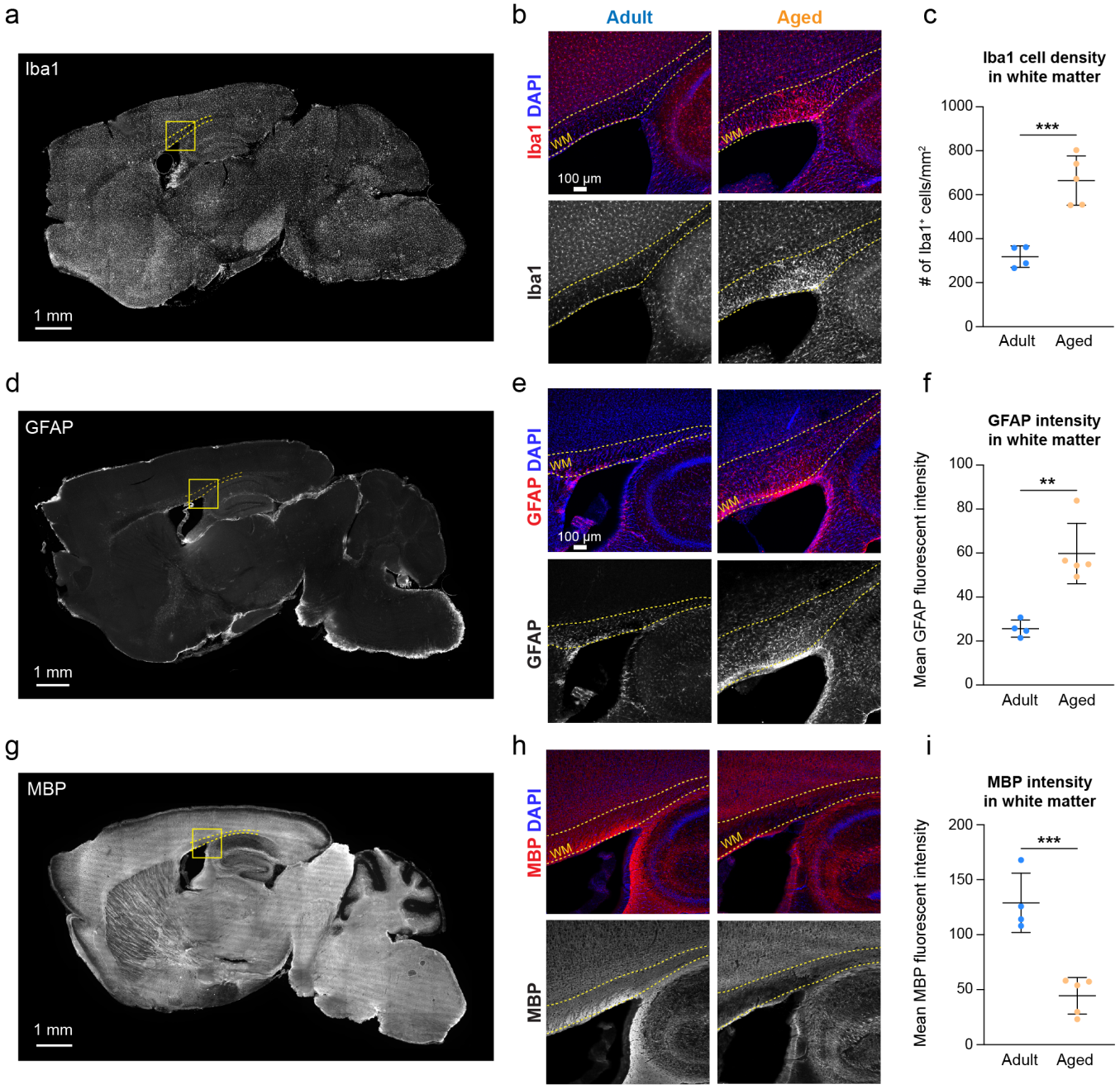

Figure 7. Gliosis and demyelination in the corpus callosum of aged mice. a, d, g. Epifluorescent images of adult mouse sagittal brain sections stained with anti-Iba1 antibody for labeling microglia (a), anti-GFAP antibody for labeling astrocytes (d), anti-MBP antibody for labeling myelin (g). **b, e, h.** Confocal images of stained sections taken in the region of the CC directly underneath the somatosensory cortex (imaged regions are marked with yellow squares in corresponding epifluorescent images from a, d and g). **c, f, i.** Plots of Iba1 positive cell density (c), mean GFAP signal intensity (f), and mean MBP signal intensity (i) in the CC analyzed in confocal images. For all plots, n=4 adult mice and 5 aged mice. Data shown as mean ± SEM. Unpaired t-test. $p < 0.001$ (c); $p = 0.002$ (f); $p < 0.001$ (i).

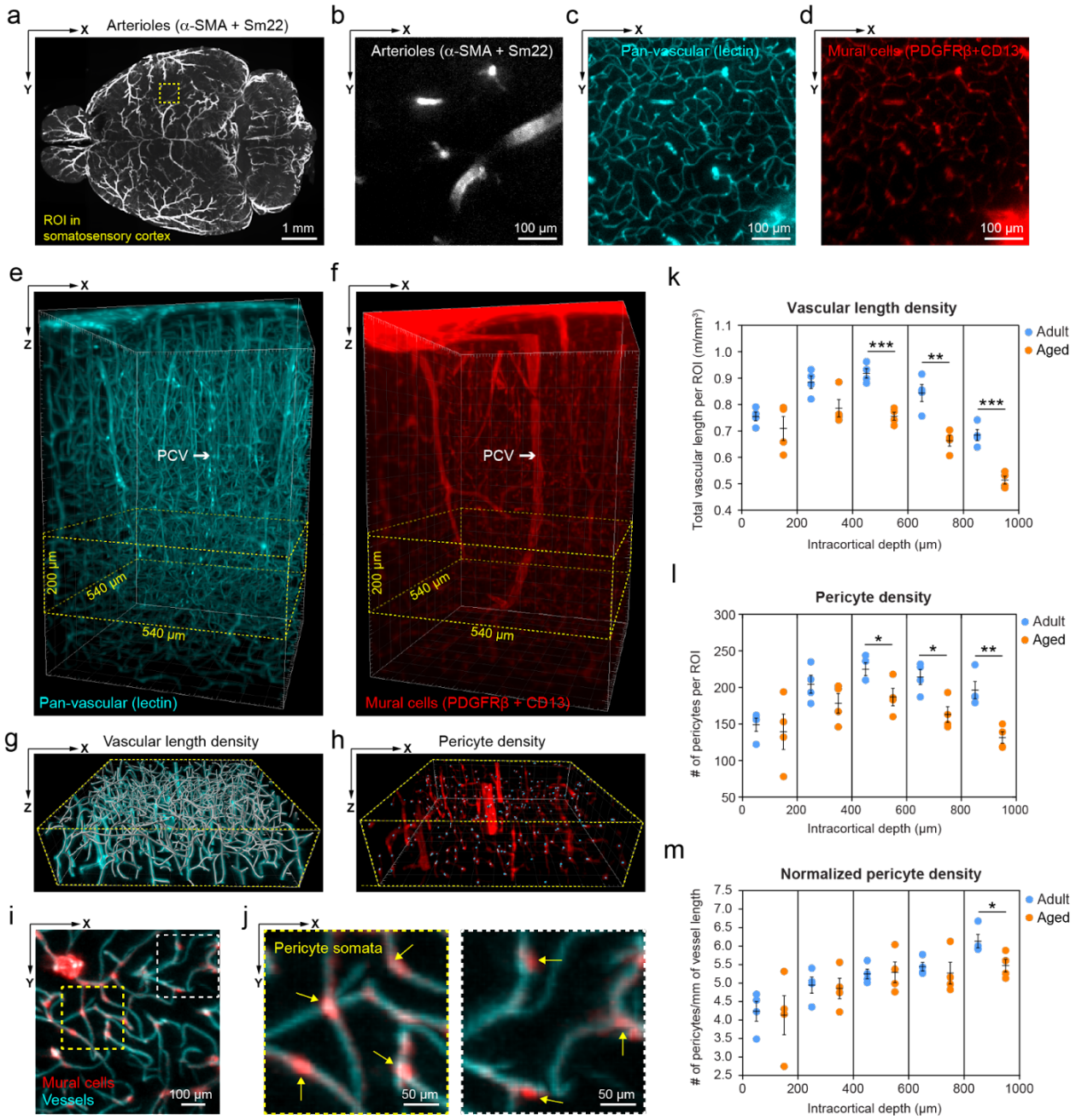

Figure 8. Reduction in vascular length and pericyte cell density in deeper tissues of aged mice. a. Maximum intensity projection of the top portion of a whole mouse brain with arterioles labeled using α-SMA + Sm22 immunostaining imaged by light-sheet microscopy. **b-d.** Top-down views of the 540 x 540 x 1000 µm (x, y, z) ROI centered on the somatosensory cortex marked with a yellow square in (a), with arterioles labeled using α-SMA + Sm22 antibodies (b), all vessels labeled using fluorescent lectin (c), and mural cells labeled using the combination of PDGFRβ and anti-CD13 antibodies (d). **e,f.** 3D side views from Imaris showing lectin (e) and mural cell (f) staining throughout the entire cortical depth. **g, h.** Examples of 200 µm ROIs from (e) and (f) (marked with dotted yellow lines) with reconstructions of all capillary segments (g, gray lines)) and annotated capillary pericyte cell somata (h, blue circles). **i.** Top-down view of the overlap between the vessels (cyan) and mural cells (red) channels. **j.** Zoomed in regions from (i) (marked with yellow squares) with annotated examples of capillary pericytes exhibiting the "bump on the log" morphology (marked with yellow arrows). **k.** Vascular length density in analyzed cortical subsections of adult and aged mice. Unpaired t-tests: 0-200 µm, p=0.385; 201-400 µm, p=0.054; 401-600 µm, p<0.001; 601-800 µm, p=0.003; 801-1000 µm, p<0.001. **l.** Pericyte density in analyzed cortical subsections of adult and aged mice. Unpaired t-tests: 0-200 µm, p=0.719; 201-400 µm, p=0.201; 401-600 µm, p=0.042; 601-800 µm, p=0.134; 801-1000 µm, p=0.004. **m.** Pericyte density in analyzed cortical subsections of adult and aged mice. Unpaired t-tests: 0-200 µm, p=0.862; 201-400 µm, p=0.804; 401-600 µm, p=0.891; 601-800 µm, p=0.606; 801-1000 µm, p=0.038. For all plots in k-m, N = 4 animals per age group. Data shown as mean ± SEM.